Monthly Notices of the ROYAL ASTRONOMICAL SOCIETY

MNRAS **509,** 1664–1680 (2022) https://doi.org/10.1093/mnras/stab3032
Advance Access publication 2021 October 30

The *Gaia*–ESO Survey: Membership probabilities for stars in 63 open and 7 globular clusters from 3D kinematics

R. J. Jackson,[1★] R. D. Jeffries,[1★] N. J. Wright,[1] S. Randich,[2] G. Sacco,[2] A. Bragaglia,[3] A. Hourihane,[4] E. Tognelli,[5,6] S. Degl'Innocenti,[5,6] P. G. Prada Moroni,[5,6] G. Gilmore,[4] T. Bensby,[7] E. Pancino,[2,8] R. Smiljanic,[9] M. Bergemann,[10] G. Carraro,[11] E. Franciosini,[2] A. Gonneau,[4] P. Jofré,[12] J. Lewis,[4] L. Magrini,[2] L. Morbidelli,[2] L. Prisinzano,[13] C. Worley,[4] S. Zaggia,[14] G. Tautvaišiene,[15] M. L. Gutiérrez Albarrán,[16] D. Montes[16] and F. Jiménez-Esteban[17]

[1]*Astrophysics Group, Keele University, Keele, Staffordshire ST5 5BG, UK*
[2]*INAF – Osservatorio Astrofisico di Arcetri, Largo E. Fermi 5, I-50125 Florence, Italy*
[3]*INAF – Osservatorio di Astrofisica e Scienza dello Spazio di Bologna, via Gobetti 93/3, I-40129 Bologna, Italy*
[4]*Institute of Astronomy, University of Cambridge, Madingley Road, Cambridge CB3 0HA, UK*
[5]*Dipartimento di Fisica 'Enrico Fermi', Universitá di Pisay, Largo Bruno Pontecorvo 3, I-56127 Pisa, Italy*
[6]*INFN, Sezione di Pisa, Largo Bruno Pontecorvo 3, I-56127 Pisa, Italy*
[7]*Lund Observatory, Department of Astronomy and Theoretical Physics, Box 43, SE-221 00 Lund, Sweden*
[8]*Space Science Data Center – Agenzia Spaziale Italiana, via del Politecnico, s.n.c., I-00133 Roma, Italy*
[9]*Nicolaus Copernicus Astronomical Center, Polish Academy of Sciences, ul. Bartycka 18, PL-00-716 Warsaw, Poland*
[10]*Max-Planck Institut für Astronomie, Königstuhl 17, D-69117 Heidelberg, Germany*
[11]*Dipartimento di Fisica e Astronomia, Università di Padova, Vicolo dell'Osservatorio 3, I-35122 Padova, Italy*
[12]*Núcleo de Astronomía, Facultad de Ingeniería, Universidad Diego Portales, Av. Ejército 441 Santiago, Chile*
[13]*INAF – Osservatorio Astronomico di Palermo, Piazza del Parlamento 1, I-90134 Palermo, Italy*
[14]*INAF – Padova Observatory, Vicolo dell'Osservatorio 5, I-35122 Padova Italy*
[15]*Institute of Theoretical Physics and Astronomy, Vilnius University, Sauletekio av. 3, 10257 Vilnius, Lithuania*
[16]*Departamento de Física de la Tierra y Astrofísíca and IPARCOS UCM, Universidad Complutense de Madrid, E-28040 Madrid, Spain*
[17]*Departamento de Astrofísica, Centro de Astrobiología (CSICINTA), Camino Bajo del Castillo s/n, Villanueva de la Canada, E-28692 Madrid, Spain*

Accepted 2021 October 11. Received 2021 October 3; in original form 2021 August 23

ABSTRACT

Spectroscopy from the final internal data release of the *Gaia*–ESO Survey (GES) has been combined with *Gaia* EDR3 to assign membership probabilities to targets observed towards 63 Galactic open clusters and 7 globular clusters. The membership probabilities are based chiefly on maximum likelihood modelling of the 3D kinematics of the targets, separating them into cluster and field populations. From 43 211 observed targets, 13 985 are identified as highly probable cluster members ($P > 0.9$), with an average membership probability of 0.993. The addition of GES radial velocities successfully drives down the fraction of false positives and we achieve better levels of discrimination in most clusters over the use of astrometric data alone, especially those at larger distances. Since the membership selection is almost purely kinematic, the union of this catalogue with GES and *Gaia* is ideal for investigating the photometric and chemical properties of clusters as a function of stellar mass, age, and Galactic position.

Key words: stars: evolution – stars: pre-main-sequence – open clusters and associations: general.

1 INTRODUCTION

The *Gaia*–ESO Survey (GES) is a large public survey programme that uses the multifibre FLAMES (Fiber Large Array Multi-Element Spectrograph; Pasquini et al. 2002) instrument on the 8-m UT2-*Kueyen* telescope of the Very Large Telescope (VLT) to perform chemical and kinematical studies of Galactic stellar populations (see Gilmore et al. 2012; Randich, Gilmore & Gaia-ESO Consortium 2013; Pancino et al. 2017). The GIRAFFE and UVES (Ultraviolet and Visual Echelle Spectrograph; Dekker et al. 2000) spectrographs attached to FLAMES, were used to obtain spectra of about 10^5 and 10^4 stars at resolving powers of $\sim$ 17 000 and $\sim$ 47 000, respectively.

About $\sim$40 per cent of the survey time was spent capturing the spectra of stars towards star clusters and associations at a range of ages (Bragaglia et al., in preparation). In total, GES either observed (or reprocessed similar archival data) and has provided chemical abundances and radial velocities for 85 open clusters and 14 globular clusters as part of the final internal Data Release 6 (hereafter GESiDR6) and these data will be made public via the ESO archive.

Clusters have a special place in astrophysics. They offer large groups of (approximately) coeval stars over a range of masses and

★ E-mail: r.j.jackson@keele.ac.uk (RJJ); r.d.jeffries@keele.ac.uk (RDJ)

evolutionary stages that can be used to test stellar models. At the same time, clusters of different ages can be used to explore or even empirically calibrate the time-dependence of various physical phenomena such as rotation, magnetic activity, or the diffusion and mixing of chemical elements. A starting point for such studies is a clean list of cluster members, or at least a list of potential members where any probability of contamination is well understood. An important consideration is to avoid using membership criteria which then bias the phenomena being tested or investigated. For example, one should not use chemical abundances as a membership indicator and then use these members to investigate the dispersion of chemical abundances within a cluster.

The work presented here follows on from Randich et al. (2018) and Jackson et al. (2020), where *Gaia* astrometry from *Gaia* DR1 and *Gaia* DR2, in the form of its first and second data releases (Gaia Collaboration 2016, 2018, respectively), was used in conjunction with spectroscopic parameters from earlier GES data releases to define samples of high probability cluster members. Jackson et al. (2020) (hereafter J20) used data available in GES internal data release 5 (GESiDR5) and *Gaia* DR2 (Lindegren et al. 2018) to provide membership probabilities for 32 clusters based on their 3D kinematics. Here, we use temperatures, gravities, and radial velocities from GESiDR6, together with astrometry from *Gaia* EDR3 (Lindegren et al. 2021), to define membership probabilities for sources in 70 clusters from GES. These comprise the full set of 60 open cluster targets in GES that were observed using the GIRAFFE spectrograph with the HR15N order-sorting filter or with UVES (two of which were 'double clusters' – pairs of clusters that are in the field of view but not kinematically related see Section 2), to which we added one archival cluster (M67) and 7 globular clusters that were also observed with GIRAFFE+HR15N and homogeneously analysed as part of the GES project.

The analysis used to determine membership probability is similar to that described in J20, however the process of selecting a list of potential cluster members has changed in some key aspects to reflect the broader mix of cluster ages and distances. In general, the clusters newly added to this study, i.e. those reported for the first time in GESiDR6, are older, more distant, and contain a higher proportion giant stars that are likely cluster members. For more distant clusters the inclusion of the third dimension of radial velocity (*RV*) from GES in stars as faint as $V \sim 19$ is critical in separating cluster members from contaminants. Overall, our aim is to provide rigorously determined membership lists, with quantitative membership probabilities, that can be used for follow-up investigations.

The paper is organized as follows: Section 2 describes the sources of data used for membership analysis, Section 3 describes the process of target selection and calculation of membership probability. In Section 4, we report the membership probabilities of individual targets for each cluster. The results are discussed in Section 5 and a summary and conclusions are provided in Section 6. Appendix A reports membership probabilities for a set of supplementary targets with three further appendices (available as supplementary material) showing plots of key results for each of the 70 clusters studied.

2 SOURCE DATA

GESiDR6 data for our analysis were taken from a library of stacked spectra for GIRAFFE HR15N and UVES observations of cluster targets and the GESiDR6 Parameter Catalogue; the latter containing values of effective temperature ($T_{\rm eff}$), gravity $\log g$, and a gravity-sensitive spectral index (γ, see Damiani et al. 2014) (plus other parameters not used here) derived by the GES Working Groups (WGs) for a large proportion of the cluster targets (see Hourihane et al., in preparation).

2.1 Cluster targets

Clusters were identified from the library of GESiDR6 stacked spectra. The data set was scanned to identify clusters where multiple targets had been observed using the GIRAFFE 665 nm (HR15N) order-sorting filter. 68 clusters were identified with unique names, two of which (see below) contained data from two kinematically separate clusters, hence our final list of 70 clusters. We note that the GES project also analysed a further 24 named open clusters. These are generally sparse clusters with few targets (only 6 with $>$50 targets) and were observed with an inhomogeneous set of spectrograph setups that did not include HR15N observations; we have not analysed those clusters in this paper.

A small number of targets (21) showed duplicate spectra, one from a GES observation and one from an archival source. In this case the latter was discarded yielding a total of 37 930 targets with GIRAFFE HR15N spectra. Scanning the data set of UVES 520 and 580 nm spectra associated with these 68 clusters identified UVES spectra for 2508 distinct targets of which 790 also had GIRAFFE HR15N spectra.

Tables 1 and 2 show lists of cluster names together with representative values of age, distance modulus, and reddening reported in the literature. Also shown are the number of unique targets observed in each cluster with GIRAFFE HR15N and/or UVES setups. Table 1 lists properties for the younger clusters ($<$0.6 Gyr). Data for subclusters NGC 2451a and NGC 2451b and for Lambda Ori and Lambda Ori B35 are shown separately since these are known to be spatially and kinematically distinct clusters. Table 2 lists the properties of 31 older open clusters with reported ages of 0.6 to 6 Gyr and 7 globular clusters with reported ages $>$10 Gyr.

Table 3 shows the full list of targets with HR15N and/or UVES spectra that are common to the WG catalogue showing the WG 'cname' together with cluster name, setup, and co-ordinates read from the spectrum metadata. The are 41 926 entries for 39 441 unique targets. Of these, 88 per cent have values of $T_{\rm eff}$ derived by the GES WGs and 67 per cent have WG values of $\log g$. Table A2 lists a further 3770 targets common to our list of 70 clusters that were observed with a variety of GIRAFFE setups but not with GIRAFFE + HR15N or UVES. In the interests of homogeneity, these targets were excluded from the main kinematic analysis but their individual membership probabilities are estimated in Appendix A.

2.2 Spectral indices

The narrow-band spectral indices γ and τ were calculated from the normalized GIRAFFE spectra using the procedure described in Damiani et al. (2014). The τ index is used to estimate an approximate value of $T_{\rm eff}$ and the index $\gamma' = \gamma + \tau/6$ is used as a proxy for $\log g$ for targets where it is not reported in the GESiDR6 WG catalogue.

2.3 Radial velocities

For GIRAFFE spectra, the radial velocities (*RV*) were read from the spectrum VELCLASS metadata. For UVES, the mean value of *RV* was taken from values reported for the upper and lower CCD spectra (Sacco et al. 2014). The offset in *RV* between HR15N and UVES measurements was estimated by comparing *RV*s measured for 790 targets observed using both setups. The results in Fig. 1 show a

Table 1. Data for younger open clusters. Columns 2–4 show ages, intrinsic distance moduli, and reddening from the literature (superscripts refer to references listed below Table 2). Columns 5–7 show the numbers of targets observed, the numbers of targets with all data required for membership analysis (see Section 2.4) and the number fitted in the membership analysis. Columns 8 and 9 show the values of distance modulus and cluster reddening calculated for high probability cluster members (see Table 3 and Section 3.5).

Cluster	Age (Myr)	$(M-m)_0$ Literature	$E(B-V)$ Literature	Number observed	Number complete	Number fitted	$(M-m)_0^c$ members	$E(B-V)^c$ members
NGC 6530	1[65]	10.48[63]	0.35[74]	1972	1907	1501	$10.60 \pm 0.02 \pm 0.09$	0.44 ± 0.10
Trumpler 14	1–3[39]	12.3[39]	0.4–0.9[39]	1111	1069	741	$12.05 \pm 0.02 \pm 0.17$	0.61 ± 0.10
Chamaeleon I	2[50]	6.02[82]	∼1[50]	708	687	170	$6.40 \pm 0.01 \pm 0.01$	0.18 ± 0.08
Rho Ophiuchus	3[26]	5.4[49]	–	311	301	72	$5.70 \pm 0.01 \pm 0.01$	0.76 ± 0.13
NGC 2264	4[80]	9.4[73]	0.07[78]	1876	1819	1408	$9.29 \pm 0.01 \pm 0.05$	0.05 ± 0.05
NGC 2244	4[15]	11.15[15]	0.48[15]	432	427	375	$10.90 \pm 0.03 \pm 0.10$	0.49 ± 0.09
Lambda Ori	6[22]	7.9[21]	0.12[20]	608	588	344	$8.00 \pm 0.01 \pm 0.03$	0.09 ± 0.04
Lambda Ori B35	6[22]	7.9[21]	0.12[20]	227	215	118	$8.00 \pm 0.01 \pm 0.03$	0.09 ± 0.02
25 Ori	6[25]	7.63[72]	0.07[72]	294	284	256	$7.71 \pm 0.01 \pm 0.02$	0.00 ± 0.02
ASCC 50	8[66]	9.64[46]	0.23[46]	1224	1192	501	$9.91 \pm 0.02 \pm 0.06$	0.28 ± 0.05
Collinder 197	13[19]	9.38[64]	0.2[64]	409	395	334	$9.94 \pm 0.02 \pm 0.06$	0.64 ± 0.07
Gamma Velorum	18[43]	7.72[42]	0.04[42]	1262	1242	497	$7.73 \pm 0.01 \pm 0.02$	0.04 ± 0.03
IC 4665	23[67]	7.69[32]	0.17[7]	567	562	298	$7.69 \pm 0.01 \pm 0.02$	0.15 ± 0.02
NGC 2232	38[3]	7.56[32]	0.03[19]	1761	1734	697	$7.52 \pm 0.01 \pm 0.02$	0.04 ± 0.03
NGC 2547	38[67]	7.97[32]	0.06[56]	477	472	269	$7.93 \pm 0.01 \pm 0.03$	0.06 ± 0.03
IC 2602	44[67]	5.91[32]	0.03[37]	1840	1817	117	$5.90 \pm 0.01 \pm 0.01$	0.04 ± 0.02
NGC 2451b	50[38]	7.84[38]	0.01[62]	1656	1635	425	$7.80 \pm 0.01 \pm 0.02$	0.10 ± 0.03
NGC 6649	50[81]	11.[81]	01.37[52]	122	121	116	$11.69 \pm 0.03 \pm 0.14$	1.43 ± 0.05
IC 2391	51[67]	5.9[32]	0.01[19]	434	426	78	$5.90 \pm 0.01 \pm 0.01$	0.03 ± 0.01
NGC 2451a	50-80[38]	6.44[32]	0.01[62]	1656	1637	352	$6.42 \pm 0.01 \pm 0.01$	0.02 ± 0.02
NGC 6405	94[47]	8.01[47]	0.14[47]	659	654	373	$8.31 \pm 0.01 \pm 0.03$	0.14 ± 0.04
NGC 6067	120[19]	10.76[19]	0.38[19]	532	531	512	$11.62 \pm 0.01 \pm 0.14$	0.34 ± 0.04
NGC 2516	125[51]	8.09[32]	0.11[75]	759	745	641	$8.07 \pm 0.01 \pm 0.03$	0.11 ± 0.03
Blanco 1	100–150[55]	6.88[32]	0.01[19]	463	446	314	$6.88 \pm 0.01 \pm 0.02$	-0.01 ± 0.03
NGC 6709	150[19]	10.16[19]	0.3[19]	684	681	551	$10.19 \pm 0.01 \pm 0.07$	0.27 ± 0.02
NGC 6259	210[54]	11.61[16]	0.66[54]	438	423	391	$11.82 \pm 0.01 \pm 0.15$	0.63 ± 0.09
NGC 6705	280[6]	11.37[43]	0.42[70]	1066	1043	977	$11.96 \pm 0.01 \pm 0.16$	0.40 ± 0.06
Berkeley 30	300[45]	13.49[45]	0.52[45]	226	224	216	$13.57 \pm 0.09 \pm 0.34$	0.51 ± 0.04
NGC 3532	300[18]	8.46[18]	0.03[18]	966	952	687	$8.40 \pm 0.01 \pm 0.03$	0.05 ± 0.02
NGC 6281	314[19]	8.86[19]	0.15[19]	251	249	63	$8.62 \pm 0.01 \pm 0.03$	0.18 ± 0.02
NGC 4815	560[30]	11.99[8]	0.7[8]	126	126	112	$12.78 \pm 0.08 \pm 0.24$	0.70 ± 0.07
NGC 6633	575[79]	7.99[32]	0.17[79]	1595	363	119	$7.99 \pm 0.02 \pm 0.03$	0.15 ± 0.04

median offset[1] of 0.2 km s^{-1}. Values of *RV* measured from UVES spectra were reduced by this value to match the GIRAFFE HR15N *RV* scale.

For GIRAFFE measurements of *RV*, the expected distribution of measurement precision is non-Gaussian, characterized by the product of a scaling constant $S_{\rm RV}$ and a Student-*t* distribution (Jackson et al. 2015), where $S_{\rm RV}$ is a function of signal-to-noise ratio (*S*/*N*), resolving power, *R*, and projected equatorial velocity ($v \sin i$). The scaling constant of uncertainty for short term repeats (e.g. spectra taken consecutively), using the same instrument set up and wavelength calibration, is given by

$$S_{\rm RV,0} = B \frac{\left(1 + ([v \sin i]/C)^2\right)^{3/4}}{(S/N)}, \quad (1)$$

where *B* is an empirically determined parameter that depends on the intrinsic stellar spectrum (largely characterized by the effective temperature) and *C* is a function of the spectrograph resolving power. For long-term repeats (e.g. spectra taken on different nights), there is an additional contribution due to variations in instrument setup and wavelength calibration, *A*, which adds in quadrature to give

$$S_{\rm RV} = \sqrt{A^2 + S_{\rm RV,0}^2}, \quad (2)$$

Analysis of 34k short term and 4.6k longer term repeat observations in the GESiDR6 data set gave the following expressions (in units of km s^{-1}) for the empirically determined parameters.

$$\begin{aligned} A &= \max(0.26, 0.04 + 13.7/(S/N)), \\ B &= 5.85 + 2.07 \tanh\left((T_{\rm eff}^d - 5000)/500\right), \\ C &= 0.895\, c/\, R, \end{aligned} \quad (3)$$

where *c* is the speed of light and $T_{\rm eff}^d$ is estimated from the spectral index τ using the polynomial function given in Section 5 of Damiani et al. (2014). These relations are well-calibrated over the temperature range $4000 < T_{\rm eff}^d < 6000$ K which is sufficient to constrain the value of *B*.

Fig. 2 shows the cumulative distribution function (CDF) of normalized measurement uncertainty, $(\Delta RV/\sqrt{2})/S_{\rm RV}$, compared to the CDF of a unit Gaussian distribution. The measured data shows a clear non-Gaussian tail with 10 per cent of targets showing $|\Delta RV/\sqrt{2}|/S_{\rm RV} > 2.6$ compared to the ∼1 per cent expected for a unit Gaussian distribution. A Student-*t* distribution of order $\nu = 3$ is a good fit to the empirical CDF of measurement uncertainty.

[1]Some of the dispersion or outliers in Fig. 1 could be due to binaries, since the GIRAFFE and UVES observations were not cotemporal.

Table 2. Data for older open and globular clusters. Columns 2–4 show ages, intrinsic distance moduli, and reddening from the literature (superscripts refer to references listed below the table). Columns 5–7 show the numbers of targets observed, the numbers of targets with all data required for membership analysis (see Section 2.2), and the number fitted in the membership analysis. Columns 8 and 9 show values of distance modulus and cluster reddening calculated for high probability cluster members. Reddenning values were not calculated for the globular clusters (see Section 3.5).

Cluster	Age (Myr)	$(M-m)_0$ Literature	$E(B-V)$ Literature	Number observed	Number complete	Number fitted	$(M-m)_0^c$ members	$E(B-V)^c$ members
Pismis18	700[35]	11.75[60]	0.5[60]	101	101	90	$12.27 \pm 0.03 \pm 0.19$	0.65 ± 0.03
Trumpler 23	800[59]	11.71[12]	0.58[4]	89	89	83	$12.20 \pm 0.03 \pm 0.18$	0.68 ± 0.04
NGC 2355	900[24]	10.92[24]	0.14[24]	208	208	204	$11.37 \pm 0.01 \pm 0.12$	0.13 ± 0.03
NGC 6802	900[76]	11.28[41]	0.84[41]	103	103	98	$12.38 \pm 0.09 \pm 0.20$	0.79 ± 0.06
Ruprecht 134	1000[12]	12.66[12]	0.5[12]	680	665	602	$12.04 \pm 0.05 \pm 0.17$	0.46 ± 0.08
Berkeley 81	1000[53]	12.39[68]	1.0[68]	203	203	171	$12.96 \pm 0.07 \pm 0.26$	0.85 ± 0.04
NGC 6005	1200[60]	12.16[60]	0.45[60]	355	353	325	$12.27 \pm 0.11 \pm 0.18$	0.49 ± 0.06
Pismis 15	1300[11]	12.31[11]	0.53[11]	235	235	224	$11.93 \pm 0.03 \pm 0.16$	0.56 ± 0.05
Trumpler 20	1400[23]	12.39[13]	0.35[13]	552	545	490	$12.88 \pm 0.02 \pm 0.25$	0.37 ± 0.03
Berkeley 44	1600[40]	12.46[41]	0.98[41]	93	92	83	$12.49 \pm 0.05 \pm 0.21$	0.90 ± 0.07
NGC 2141	1800[23]	13.12[23]	0.4[23]	853	846	801	$13.37 \pm 0.02 \pm 0.31$	0.35 ± 0.04
Czernik 24	2000[31]	13.22[31]	0.54[48]	346	343	302	$13.18 \pm 0.07 \pm 0.28$	0.65 ± 0.03
Haffner 10	2000[19]	12.84[19]	0.55[19]	460	457	428	$12.94 \pm 0.05 \pm 0.25$	0.52 ± 0.05
NGC 2158	2000[10]	13.49[19]	0.36[19]	616	598	571	$13.20 \pm 0.03 \pm 0.29$	0.48 ± 0.04
NGC 2420	2200[69]	11.97[71]	0.05[2]	562	557	520	$12.03 \pm 0.01 \pm 0.17$	0.04 ± 0.03
Berkeley 21	2200[83]	13.98[83]	0.74[83]	744	738	574	$14.27 \pm 0.17 \pm 0.48$	0.66 ± 0.06
Berkeley 73	2300[19]	14.49[19]	0.1[19]	76	75	70	$14.65 \pm 0.19 \pm 0.57$	0.22 ± 0.05
Berkeley 22	2400[27]	13.8[27]	0.72[27]	395	395	352	$14.16 \pm 0.12 \pm 0.45$	0.58 ± 0.07
Czernik 30	2800[36]	14.03[36]	0.24[36]	226	226	193	$14.49 \pm 0.12 \pm 0.53$	0.31 ± 0.03
Berkeley 31	2900[17]	14.4[17]	0.19[17]	616	614	499	$14.50 \pm 0.19 \pm 0.53$	0.10 ± 0.07
Berkeley 75	3000[19]	14.96[19]	0.08[19]	75	74	64	$14.75 \pm 0.18 \pm 0.59$	0.10 ± 0.03
Loden 165	3000[9]	11.39[9]	0.25[9]	388	387	333	$11.79 \pm 0.07 \pm 0.15$	0.21 ± 0.06
NGC 6253	3000[5]	10.9[5]	0.28[5]	294	235	227	$11.15 \pm 0.01 \pm 0.11$	0.24 ± 0.03
Messier 67	3500[32]	9.73[32]	0.04[32]	131	131	130	$9.67 \pm 0.01 \pm 0.06$	0.05 ± 0.01
NGC 2425	3600[34]	12.63[34]	0.28[34]	528	525	481	$12.69 \pm 0.02 \pm 0.23$	0.35 ± 0.04
NGC 2243	3800[1]	12.96[1]	0.05[1]	703	701	614	$13.29 \pm 0.02 \pm 0.30$	0.04 ± 0.04
Berkeley 36	4000[57]	13.84[57]	0.3[57]	739	737	672	$13.44 \pm 0.08 \pm 0.32$	0.54 ± 0.05
Trumpler 5	5000[61]	11.9[61]	0.6[61]	1138	1132	1098	$12.61 \pm 0.02 \pm 0.22$	0.63 ± 0.06
Berkeley 32	5900[29]	12.5[77]	0.15[77]	389	385	348	$12.72 \pm 0.02 \pm 0.23$	0.16 ± 0.04
Berkeley 39	6000[44]	12.9[44]	0.11[8]	899	897	832	$13.29 \pm 0.02 \pm 0.30$	0.10 ± 0.05
ESO 92-05	6000[58]	15.19[58]	0.17[58]	212	210	114	$16.06 \pm 0.30 \pm 1.16$	0.06 ± 0.10
NGC 1261	10200[28]	16.06[33]	0.01[33]	80	80	66	$17.21 \pm 0.29 \pm 2.58$	–
NGC 362	10400[28]	14.84[14]	0.06[14]	148	147	133	$15.37 \pm 0.12 \pm 0.81$	–
NGC 2808	10800[28]	14.91[33]	0.22[33]	289	269	191	$15.39 \pm 0.04 \pm 0.82$	–
NGC 1904	11100[28]	15.56[33]	0.01[33]	71	71	62	$16.11 \pm 0.09 \pm 1.19$	–
NGC 6752	11800[28]	13.01[33]	0.04[33]	353	322	297	$13.30 \pm 0.04 \pm 0.30$	–
NGC 5927	12700[28]	14.43[33]	0.45[33]	124	123	88	$15.39 \pm 0.18 \pm 0.82$	–
NGC 104	13100[28]	13.45[14]	0.05[14]	311	301	296	$13.41 \pm 0.04 \pm 0.32$	–

Notes. [1]Anthony-Twarog, Atwell & Twarog (2005) [2]Anthony-Twarog et al. (2006) [3]Binks et al. (2021) [4]Bonatto & Bica (2007) [5]Bragaglia et al. (1997) [6]Cantat-Gaudin et al. (2014) [7]Cargile, James & Jeffries (2010) [8]Carraro & Ortolani (1994) [9]Carraro, Patat & Baumgardt (2001) [10]Carraro, Girardi & Marigo (2002) [11]Carraro et al. (2005) [12]Carraro et al. (2006) [13]Carraro, Costa & Ahumada (2010) [14]Carretta et al. (2000) [15]Chen, de Grijs & Zhao (2007) [16]Ciechanowska et al. (2006) [17]Cignoni et al. (2011) [18]Clem et al. (2011) [19]Dias et al. (2002) WEBDA [20]Diplas & Savage (1994) [21]Dolan & Mathieu (1999) [22]Dolan & Mathieu (2002) [23]Donati et al. (2014) [24]Donati et al. (2015) [25]Downes et al. (2014) [26]Erickson et al. (2011) [27]Di Fabrizio et al. (2005) [28]Forbes & Bridges (2010) [29]Friel, Jacobson & Pilachowski (2010) [30]Friel et al. (2014) [31]Froebrich et al. (2010) [32]Gaia Collaboration et al. (2018) [33]Harris (1996) GCDB [34]Hasegawa, Sakamoto & Malasan (2008) [35]Hatzidimitriou et al. (2019) [36]Hayes et al. (2015) [37]Hill & Perry (1969) [38]Hünsch & Weidner (2003) [39]Hur, Sung & Bessell (2012) [40]Jacobson et al. (2016) [41]Janes & Hoq (2011) [42]Jeffries et al. (2009) [43]Jeffries et al. (2017) [44]Kassis et al. (1997) [45]Kharchenko et al. (2013) [46]Kharchenko et al. (2013) [47]Kılıçoğlu et al. (2016) [48]Kim et al. (2005) [49]Loinard et al. (2008) [50]Luhman (2007) [51]Lyra et al. (2006) [52]Madore & van den Bergh (1975) [53]Magrini et al. (2015) [54]Mermilliod et al. (2001) [55]Moraux et al. (2007) [56]Naylor & Jeffries (2006) [57]Ortolani et al. (2005) [58]Ortolani, Bica & Barbuy (2008) [59]Overbeek et al. (2017) [60]Piatti et al. (1998) [61]Piatti, Clariá & Ahumada (2004) [62]Platais et al. (2001) [63]Prisinzano et al. (2005) [64]Prisinzano et al. (2018) [65]Prisinzano et al. (2019) [66] Prisinzano L. - private com. [67]Randich et al. (2018) [68]Sagar & Griffiths (1998) [69]Salaris, Weiss & Percival (2004) [70]Santos, Bonatto & Bica (2005) [71]Sharma et al. (2006) [72]Suárez et al. (2017) [73]Sung, Bessell & Lee (1997) [74]Sung, Chun & Bessell (2000) [75]Sung et al. (2002) [76]Tang et al. (2017) [77]Tosi, Bragaglia & Cignoni (2007) [78]Turner (2012) [79]van Leeuwen (2009) [80]Venuti et al. (2018) [81]Walker & Laney (1987) [82]Whittet et al. (1997) [83]Yong, Carney & Friel (2012).

The measurement uncertainties of UVES *RV* values are calculated from the difference in *RV* measured from the upper and lower spectra, $\Delta RV/\sqrt{2}$, in quadrature with a constant term of $0.4\,\mathrm{km\,s^{-1}}$ representing the uncertainty in wavelength calibration (Sacco et al. 2014). The median uncertainty in UVES and GIRAFFE RV measurements is $<0.5\,\mathrm{km\,s^{-1}}$.

The reader should be aware that the *RV* values reported here will differ from the public GES *RV* catalogue delivered to ESO in two

Table 3. Membership probabilities for GESiDR6 cluster targets. Columns 1 to 5 show the GESiDR6 target names, cluster and filter and co-ordinates. Targets flagged 0 are included in the maximum likelihood analysis (see Section 3.1). Column 7 to 9 show the measured *RV* and scaling constant for empirical uncertainty (see Section 2.3), *Gaia* cross-matched ID and *G* magnitude. Columns 10 and 11 show $T_{\rm eff}^{p}$ and K_S^{p} data (which includes estimated values for some targets) used to determine log *L* and mass for the likelihood analysis (see Section 3.3). The final columns show the probability that the target is a member of its given cluster using the full data set, $P_{\rm 3D}$, or the same probability computed using a data set filtered to remove targets with suspect *Gaia* data, $P_{\rm QG}$. Targets with a membership probability of −1 were excluded from the membership analysis. A sample of the table is shown here. The full table is available as supplementary material.

Target cname	cluster DB name	setup (nm)	RA (deg)	Dec (deg)	Flag	*RV* (km s^{-1})	*Gaia* ID	*G* (mag)	$T_{\rm eff}^{p}$ (K)	K_S^{p} (mag)	log *L*	Membership $P_{\rm 3D}$	$P_{\rm QG}$
07515457-6047568	NGC2516	665	117.97737	−60.79911	0	6.84 ± 0.55	ID5290899847497012352	15.75	4369	12.87	-0.92	0.5674	0.5542
07515966-6047220	NGC2516	665	117.99858	−60.78944	0	25.90 ± 0.31	ID5290899881856756224	15.96	4233	12.89	-0.96	0.9991	0.9991
07520129-6043233	NGC2516	665	118.00538	−60.72314	0	14.60 ± 1.33	ID5290912354441812352	17.42	3767	13.96	-1.46	0.0000	0.0000
07520389-6050116	NGC2516	665	118.01621	−60.83655	0	25.54 ± 0.31	ID5290898816704856320	15.93	4256	12.87	-0.95	0.9997	0.9997
07521002-6044245	NGC2516	665	118.04175	−60.74014	0	25.63 ± 0.33	ID5290912113923645952	16.09	4153	13.17	-1.09	0.9998	0.9998
07523629-6046405	NGC2516	665	118.15121	−60.77792	0	31.33 ± 0.79	ID5290899396521946240	17.44	3883	13.98	-1.45	0.0000	0.0000

Note. Values of $P_{\rm 3D}$ and $P_{\rm QG}$ are not reported for Loden 165 since the maximum-likelihood calculation failed for this cluster (see Section 5.1).

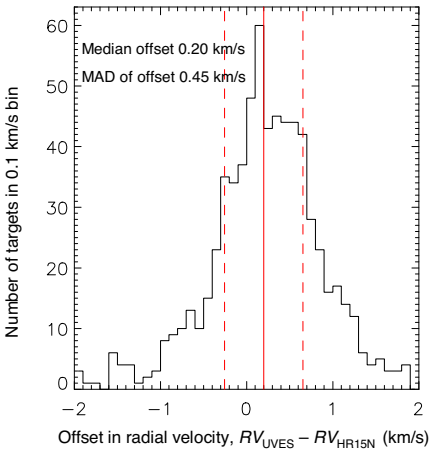

Figure 1. Histogram of the offset between UVES and GIRAFFE HR15N measurements of *RV* for targets that have repeat measurements.

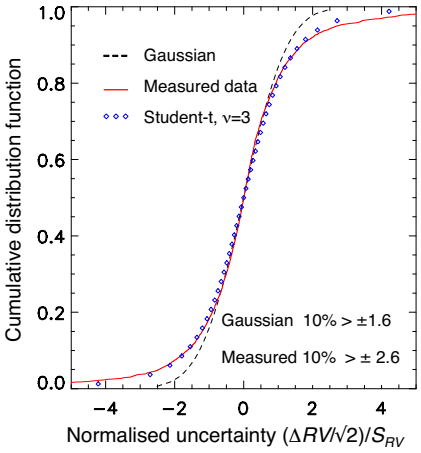

Figure 2. CDF of the normalized value of empirical uncertainty in GIRAFFE HR15N measurements of *RV* (see Section 2.3).

ways (see Hourihane et al., in preparation). (i) Most of our *RV*s come from the GIRAFFE+HR15N spectra and these have been shifted by +0.09 km s^{-1} in the construction of the GES *RV* catalogue to more closely match the *RV* values of standard stars. This is a simple shift to all the velocities, that was not applied here, and has no impact on the membership analysis. (ii) In the interests of homogeneity we quote the *RV* from a single spectrum (the GIRAFFE+HR15N value is preferred over UVES) and make no attempt to average the *RV* values or identify variability for the ∼5 per cent of stars that were observed with both GIRAFFE+HR15N, and with UVES or in archival data.

2.4 Near infrared and *Gaia* data

Target coordinates were cross-matched (in a 2 arcsec radius) with the 2MASS (Skrutskie et al. 2006), VISTA VHSDR6 (McMahon et al. 2013), and VVVDR4 (Minniti et al. 2010) catalogues to obtain K_S magnitudes on the 2MASS system. K_S data from the VISTA catalogues were used in preference to 2MASS data on 7416 occasions where $K_S > 13$ or the 2MASS quality flag for K_S was not 'A'.

Targets listed in Table 3 were cross-matched with the *Gaia* EDR3 catalogue to determine their astrometric properties and principle

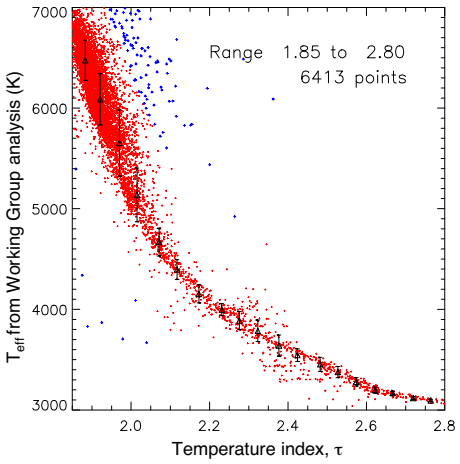

Figure 3. GESiDR6 Working Group $T_{\rm eff}$ versus temperature index τ. Triangles show the median value of $T_{\rm eff}$ in bins of τ. The red points are WG data used to define the median value in each, blue crosses are outliers rejected from the fit.

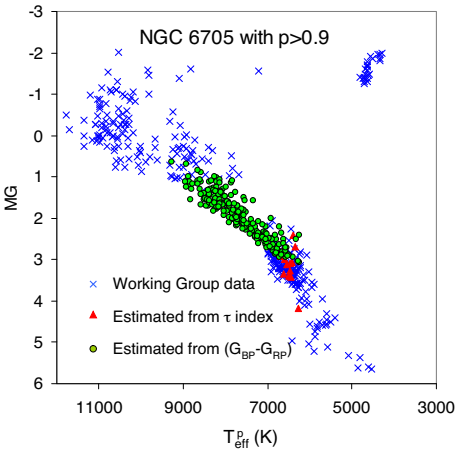

Figure 4. *Gaia G* magnitude versus $T^p_{\rm eff}$ for targets in open cluster NGC 6705 later identified as cluster members with $P > 0.9$. Blue crosses show targets with WG values of $T^p_{\rm eff}$, red triangles show stars where $T^p_{\rm eff}$ is estimated from the spectral index τ, green circles are targets where $T^p_{\rm eff}$ is estimated from their $(G_{\rm BP} - G_{\rm RP})$ colour.

photometric properties (G magnitude and $G_{\rm BP} - G_{\rm RP}$ colour) using the *Gaia* ID given in the GESiDR6 parameter catalogue. There were 435 targets missing parallax, proper motion or G magnitude data. These were flagged as incomplete (Flag $= -1$ in Table 3) and not used in the analysis. In NGC 6633, 1253 erroneous targets observed before the JD2456852 d were also flagged as -1 and excluded from the analysis (see J20 for an explanation).

2.5 Approximate values of γ, $T_{\rm eff}$, and K_S

Values of $\log g$ or γ', $T_{\rm eff}$ and K_S were required for all targets used in the membership analysis in order to identify giants and estimate target luminosities and masses to model the effects of binarity on cluster membership probability. Approximate values of $T^p_{\rm eff}$ and K^p_S were calculated where WG values were not available. If both $\log g$ and γ were not available in the WG data then a value of γ was calculated directly from its spectrum (see Section 2.2).

Where no WG value of $T_{\rm eff}$ was available an approximate value, $T^p_{\rm eff}$, was found from the temperature index τ (Section 2.2) using the calibration curve in Fig. 3, valid in the range $3100 < T_{\rm eff} < 6700$ K. If no WG data was available for hotter stars, an approximate value of $T^p_{\rm eff}$ was estimated from the $(G_{\rm BP} - G_{\rm RP})$ colour using Pisa model $(G_{\rm BP} - G_{\rm RP})_0$ to $T_{\rm eff}$ relations (Tognelli, Prada Moroni & Degl'Innocenti 2011), updated to reflect *Gaia* EDR3 filter characteristics, together with the calculated cluster reddening in Tables 1 and 2 and $R_{\rm Bp\text{-}Rp} = 1.34$ (Casagrande & VandenBerg 2018). Fig. 4 shows results in a typical cluster where the τ index and $(G_{\rm BP} - G_{\rm RP})$ colour data have been used to supplement WG $T_{\rm eff}$ data to provide a working value of $T^p_{\rm eff}$ in Table 3 for >99.5 per cent of valid targets.

K_S data are available from 2MASS and/or VISTA sources for 95 per cent of targets. For the remainder, Pisa model isochrones were used to estimate an approximate value, K^p_S in Table 3, from *Gaia G* magnitude and $(G_{\rm BP} - G_{\rm RP})$ colour using the values of age, $(M - m)^c_0$ and $E(B - V)^c$ in Tables 1 and 2. For this calculation we used $R_G = 2.50$ (Chen et al. 2019), $R_{Ks} = 0.35$ (Yuan, Liu & Xiang 2013), and the relation $(G - K_S)_0 = -0.1885 + 2.092(G_{\rm BP} - G_{\rm RP})_0 - 0.1345(G_{\rm BP} - G_{\rm RP})^2_0$ (Busso et al. 2018).

Tables 1 and 2 show the numbers of targets observed and the number with the complete data required to estimate cluster membership (i.e. *Gaia* data and values of $T^p_{\rm eff}$, and K^p_S). 95 per cent of the targets observed have the required data. Tangential velocities (and their uncertainties) were calculated from proper motions for these targets, assuming potential cluster members are at a common distance:

$$V_{\rm RA} = 4.74 d_c \, {\rm pm}_{\rm RA} \, ,$$
$$V_{\rm Dec} = 4.74 d_c \, {\rm pm}_{\rm Dec} \, , \quad (4)$$

where $\rm pm_{RA}$ and $\rm pm_{Dec}$ are the proper motions in units of mas yr^{-1}, and d_c is the cluster distance in pc calculated from the distance modulus for high probability cluster members ($(M - m)^c_0$ in Tables 1 and 2).

3 CALCULATED PARAMETERS

3.1 Selecting potential cluster members

The list of valid targets was screened to remove targets that are highly unlikely to be cluster members. This process is particularly important for the younger clusters where a large fraction of observed targets are background giants, which can easily be identified from their $\log g$ and parallax. Targets meeting one or more of the following criteria were filtered from the wider sample.

(i) **Background giants by $\log g$**: Stars in clusters aged <1 Gyr which have $\log g \leq 3.4$, $4000 < T^p_{\rm eff}/{\rm K} < 7000$ and with a parallax smaller (by at least 2σ) than a value corresponding to the intrinsic distance modulus of the cluster +2 mag. These giants are flagged as type 1 in Table 3.

(ii) **Background giants by γ'**: Stars where $\log g$ is undefined but the modified index $\gamma' \geq 1.335$ (see Section 2.2) and that meet the other conditions of the first criteria. These are flagged type 2 in Table 3.

(iii) **Background targets by parallax**: Stars with a *Gaia* parallax smaller, by at least 4σ, than a value corresponding to the intrinsic distance modulus of the cluster +2 mag. These are flagged type 3 in Table 3. For two clusters (ASCC 50 and NGC 6281) it was necessary to reduce the margin of this criteria to cluster distance modulus + 1 mag, in order to obtain a satisfactory peak in log likelihood in the membership analysis (see Section 5.1).

(iv) **Targets with a large velocity offset relative to other cluster members**; Stars with $V_{\rm RA}$, $V_{\rm Dec}$, or RV outside a window of $\pm 75\,{\rm km\,s^{-1}}$ centred on the median velocity of the remaining targets. This rejected targets with bad velocity data whilst retaining almost the entire velocity spectrum of the field population.

Tables 1 and 2 show the numbers of targets in each cluster that remain after the screening process and that are used for the membership analysis.

3.2 Filtering by quality of the astrometric solution

For the principle analysis in this paper the *Gaia* EDR3 data are accepted if there are reported values of G magnitude, parallax, and proper motions. An alternative approach examined in J20 is to filter out targets which were observed for only a low number of visibility periods, NPER < 8 (Arenou et al. 2018), and those showing a high renormalized unit weighted error, RUWE > 1.4 (Lindegren et al. 2018). Applying this additional filter reduces the number of targets fitted in the membership analysis by ∼9 per cent. The effect of applying this additional filter is discussed in section 5.2.

3.3 Target luminosity and mass

Stellar luminosities ($\log L$) in Table 3 were calculated from the K_S^p magnitude using bolometric corrections interpolated from the $T_{\rm eff}^p$ and photometry reported for updated solar metallicity Pisa model isochrones (Tognelli et al. 2011). Target masses were used solely to model the distribution of binary velocities in the membership analysis (see J20) and these were estimated from $\log L$ using the same Pisa model isochrones. The predicted mass at the turn-off was adopted as the maximum mass since giants will not be much more massive than this. Note that velocity perturbations due to the modelled binarity in the membership analysis scale only as $M^{1/3}$, so mass uncertainties are of little importance.

3.4 Probability of cluster membership

Tangential velocities, RVs and their associated measurement uncertainties and target masses were used to estimate membership probabilities for individual cluster targets using the maximum-likelihood method originally proposed by Pryor & Meylan (1993) and later updated by Cottaar, Meyer & Parker (2012) to include the effect of binarity. Simulated velocity distributions of cluster and field stars are represented by Gaussians whose intrinsic width is then broadened due to the effects of individual uncertainties and, in the case of RV, a model for the perturbations caused by a fraction of binary systems following the method described by Cottaar et al. (2012). The adopted parameters for the binary distribution come from the binary survey of Raghavan et al. (2010): a binary fraction, $f_{\rm B} = 0.46$, a lognormal period distribution with a mean log period $= 5.03$ (in days) and dispersion 2.28 dex, and a flat mass ratio distribution for $0.1 < q < 1$. Further detail and a discussion of the effect of these assumptions and of the possibility that binarity perturbs the proper motion distribution is given in J20.

The maximum-likelihood calculation used to fit the cluster/field populations for each cluster and assign membership probabilities is detailed in J20. In brief, it was done in two stages. First the mean velocity and dispersion of the background population of field stars was characterized for each velocity component using a series of 1D maximum-likelihood analyses. These results were then used in a full 3D analysis to determine expectation values of mean velocity, the intrinsic dispersion for each velocity component, and the fraction of targets that are cluster members. The uncertainty in RV is independent of the uncertainty in proper motions allowing the 3D likelihood, $\mathcal{L}_{\rm 3D}$ to be calculated as the product of the likelihood of fit in RV, $\mathcal{L}_{\rm RV}$ and the fit in proper motion space, $\mathcal{L}_{\rm pm}$. Calculation of $\mathcal{L}_{\rm RV}$ takes account of the effects of binarity on measurement uncertainty. Calculation of $\mathcal{L}_{\rm pm}$ takes account of the correlated uncertainty between $V_{\rm RA}$ and $V_{\rm Dec}$, using the covariance matrix element 'pmRApmDEcor' in the *Gaia* EDR3 data set to define a weight matrix for each target to normalize the uncertainties in proper motion velocities (see Appendix A of Gaia Collaboration 2016).

A 1D model for each velocity component, consisting of the sum of two Gaussian distributions – one representing the cluster and one the background, was assumed for the majority of clusters. In these cases the 1D likelihood was determined as a function of five free parameters: the intrinsic velocity and dispersion of the cluster and background populations and the overall fraction of the target population that are cluster members. A more complex model, comprising three Gaussian distributions, one representing the cluster and two representing the distribution of background stars, was used to model 10 of the clusters and gave a significantly higher maximum log likelihood. In 4 cases this was expected since the clusters Gamma Vel (Jeffries et al. 2014), NGC 2547 (Sacco et al. 2015), and the cluster pair NGC 2451a and NGC 2451b (Hünsch & Weidner 2003) were previously known to lie close in velocity space to a second velocity grouping. We found 6 further clusters where the background population is best represented by the sum of two Gaussian distributions. These are NGC 6530, NGC 2264, NGC 2232, ASCC 50, NGC 2244, and NGC 6405.

Membership probabilities of individual targets are calculated as the expectation value of being a cluster member evaluated over the full grid of model velocities, velocity dispersions, and fractional membership weighted according to the total likelihood summed over all potential cluster members.

An independent 2D calculation of the probability of cluster membership ($P_{\rm 2D}$) was made using just the $V_{\rm RA}$ and $V_{\rm Dec}$. In most cases this was successful in that a clear maximum was found in likelihood space. The 2D calculation was unsuccessful (i.e. no maximum was found) for 6 of the more distant/sparsely populated clusters (ASCC 50, NGC 6005, Haffner 10, Berkeley 21, Berkeley 31, and Loden 165). Results of the 2D and 3D analyses are compared in Section 5.2.

3.5 Distance modulus and reddening

Initial likelihood analyses of cluster membership were made using the literature values of distance modulus and reddening in Tables 1 and 2. Taking the initial set of cluster members with $P_{\rm 3D} > 0.9$, the analyses were then iterated to determine the values of $(M-m)_0^{\rm c}$ and $E(B-V)^{\rm c}$ shown in the right-hand columns of the same tables. $(M-m)_0^{\rm c}$ is estimated from the weighted mean parallax of cluster members taking account of the intrinsic dispersion of the cluster (see Section 3.4 of J20). A systematic error equivalent to 0.03 mas in parallax is shown to account for possible correlated errors in the parallax zero-point (Lindegren et al. 2021).

A mean $E(B-V)^{\rm c}$ was estimated by comparing the $G-K_s$ of cluster members with Pisa, solar metallicity, model isochrone predictions of $(G-K_s)_0$ at the WG values of $T_{\rm eff}$. To account for the effects of binaries we used the median value from bluest half of the data, assuming their colours to be representative of single stars. The resulting $E(G-K_s)$ was converted to $E(B-V)$ using the extinction coefficients from Yuan et al. (2013) and Chen et al.

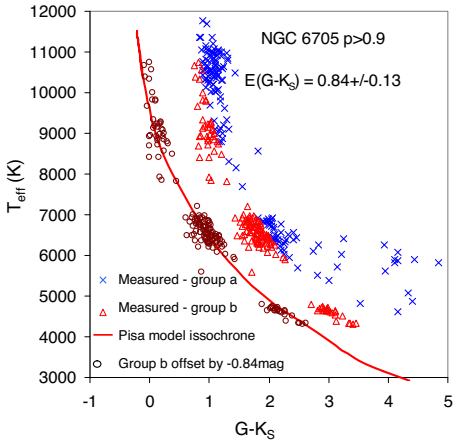

Figure 5. Evaluation of $E(G - K_S)$ for NGC 6705. The triangles and crosses show measured values of $T_{\rm eff}$ as a function of $(G - K_S)$. Group b represents probable single stars and their median offset in colour relative to the Pisa model isochrone is taken to be the reddening – $E(G - K_s) = 0.84$ in this case. The open circles show the effect of subtracting 0.84 from the $G - K_s$ values of group b.

(2019). Fig. 5 shows an example of this process for NGC 6705. The use of solar metallicity isochrones is considered acceptable for the open clusters which have metallicities in the range $-0.5 <$ [M/H] < 0.3. This is not the case for globular clusters which have lower metallicities and in those cases we adopt the literature value of $E(B - V)$ throughout.

$(M - m)_0^c$ and $E(B - V)^c$ are effectively scaling constants in the likelihood analysis, changing them has no direct effect on the membership probabilities. Both parameters have a very weak, indirect effect on membership probabilities, since they only affect the estimated mass used to determine the *RV* offsets of binary stars; but even then, the binary *RV* offsets scale only as $M^{1/3}$.

4 RESULTS

4.1 Measured data and model fits

As an example of the results, Fig. 6 shows the outcomes of the maximum-likelihood analysis for the relatively distant (d_c = 2.5 kpc) open cluster NGC 6705. Figs 6(a)–(c) show histograms of each velocity component in 1 km s^{-1} bins, with a black curve indicating a 'best fit' probability distribution based on the maximum-likelihood values of cluster central velocity and intrinsic dispersion and a median value of observational uncertainty. The observational uncertainty in *RV* reflects the combined effects of the non-Gaussian distribution of measurement uncertainty in *RV* (see Section 2.3) and the *RV* offsets calculated for a proportion of randomly oriented binary systems (see Section 3.4).

Fig. 6(d) shows the fraction of targets with P_{3D} above a threshold level versus that threshold level. Text on the plot indicates the proportion of targets that are considered likely cluster members with P_{3D} above a threshold value of 0.9. The sharpness of the 'step' indicates how well the analysis discriminates between members and background stars. For example in NGC 6705, 57 per cent of targets are identified as likely ($P_{3D} > 0.9$) members, 39 per cent as probable background stars ($P_{3D} < 0.1$), with only 4 per cent having intermediate values and effectively unresolved membership.

Similar figures for each cluster are shown in Appendix B (available on-line only) in order of the cluster age shown in Tables 1 and 2.

4.2 Cluster velocity and dispersion

Fig. 7 shows log likelihood as a function of the three central velocities and intrinsic velocity dispersions for NGC 6705. The dotted lines mark the 1σ level (a log likelihood increment of -0.5 relative to the maximum value). Text on the plots show the maximum-likelihood value of each parameter and values at the upper and lower 1σ levels. The range explored for each parameter is set to be greater than $\pm 5\sigma$ from the maximum-likelihood value of that parameter, but with a minimum value of zero for the velocity dispersion. Similar figures for each cluster are shown in Appendix C in age order (available on-line only).

NGC 6705 is a well-defined cluster with almost 1000 targets, over 50 per cent of which are probable cluster members. These produce clearly identified likelihood peaks for each of the cluster velocity parameters. For more distant clusters and those with small numbers of likely cluster members these curves can be broader and in a few cases become irregular. ESO 92-05 shows a secondary peak in the likelihood distribution of *RV* dispersion, although the dominant peak is readily identified. For Loden 165, the 3D analysis fails to find any peak at all in the likelihood distribution of D_c, invalidating calculations of membership probability for this cluster (see Section 5.1).

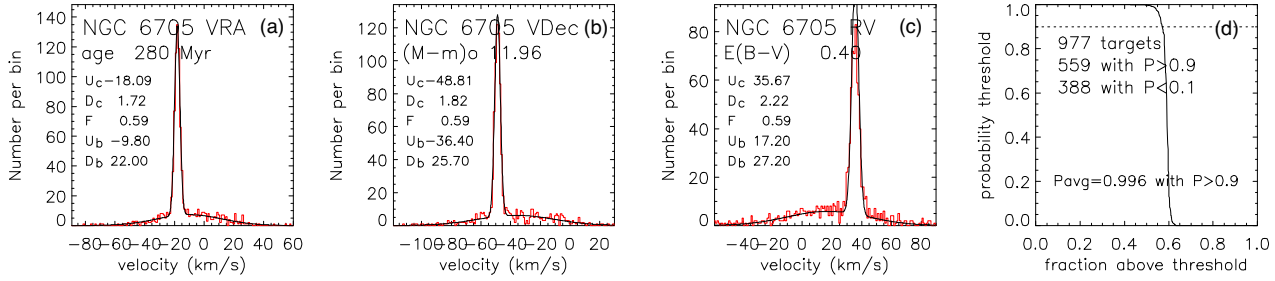

Figure 6. Results of the 3D maximum-likelihood analysis of NGC 6705. Plots (a), (b), and (c) show histograms of the three velocity components ($V_{\rm RA}$, $V_{\rm Dec}$, and *RV*), together with model probability distributions evaluated at the maximum-likelihood values of the fitted parameters, using a median measurement uncertainty. The text shows the best-fitting values of cluster velocity (U_c, in km s^{-1}), intrinsic dispersion of the cluster velocity (D_c), the fraction of objects assigned to the cluster population (F), and the velocity and dispersion of the (primary) background population (U_b, D_b). (d) The fraction of targets with membership probability, P_{3D} above a threshold level versus the threshold level.

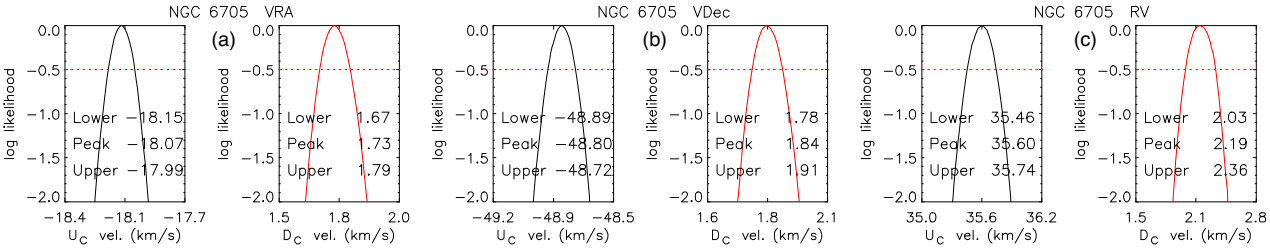

Figure 7. Likelihood of cluster properties for NGC 6705. Plots (a), (b), and (c) show the variation in log likelihood of the mean cluster velocity, U_c and the intrinsic cluster dispersion D_c for each velocity component. Text on the plots shows the peak and upper and lower 1σ probability values of the plotted parameter.

The likelihood curves were used to determine the mean and rms values of cluster central velocity and intrinsic dispersion shown in Tables 4 and 5. These values are the result of fitting the measured velocities in a fixed co-ordinate system to determine the probability of cluster membership. They do not necessarily characterize the true shape of the cluster in velocity space. This might require a more general model of the cluster that allows for free rotation of the cluster axes, bulk rotation of the cluster and, depending on the size of the cluster, modelling of 'perspective expansion' (van Leeuwen 2009; Kuhn et al. 2019), none of which are crucial to the cluster membership calculations. In addition, the assumed unresolved binary fraction will affect the inferred intrinsic velocity dispersion in *RV*, but probably has a negligible influence on the tangential velocity dispersions (see Section 5.4 of J20).

4.3 Target membership probabilities

Membership probabilities, P_{3D}, for individual targets in each cluster are reported in Table 3, which contains 41 926 entries for 39 441 unique targets of which 12 110 are $P_{3D} > 0.9$ cluster members. Targets with a membership probability of -1 were not included in the maximum-likelihood analysis. Membership probabilities, P_{QG}, are also given for the slightly smaller sample of potential cluster members, where targets with potentially unreliable *Gaia* data were excluded from the analysis (see Section 3.2).

Targets identified as cluster members were used to calculate the distance moduli and reddening values – $(M-m)_o^c$, and $E(B-V)^c$ – shown in Tables 1 and 2 (see Section 3.5). The numbers of targets in each cluster with $P_{3D} > 0.9$ and $P_{QG} > 0.9$ are also reported in Tables 4 and 5.

Membership probabilities of supplementary targets observed with alternate GIRAFFE setups are discussed in Appendix A. These targets are not included in the main cluster kinematic analyses and their membership probabilities are calculated as the expectation value of their being members of the cluster as defined only by the Giraffe + HR15N and UVES targets. From a list of 3770 additional targets in Table A2, 1875 are identified as $P_{3D} > 0.9$ cluster members.

4.4 Properties of potential and likely cluster members

Fig. 8 shows four plots of targets and likely cluster members in NGC 6705. Similar figures for all clusters, in age order, are provided in Appendix D (available on-line only).

(i) Fig. 8(a) shows a Hertzsprung–Russell (HR) diagram for all the targets used in the analysis (those flagged ≥ 0 in Table 3). Targets identified as background giants or distant background stars (flagged > 0) are identified separately as blue crosses.

(ii) Fig. 8(b) shows the tangential velocity components V_{RA} versus V_{Dec} for ($P_{3D} > 0.9$) cluster members. Ellipses represent one and two times the intrinsic cluster dispersion with error bars indicating their uncertainties. This plot also shows a histogram of the number of members versus distance modulus over a $\pm$ 1 magnitude range relative to the cluster centre (see scale above the plot). The histogram shows a relatively broad peak centred on 11.9 mag, indicating that at this distance, parallax measurements are of limited value in determining the probability of cluster membership.

(iii) Fig. 8(c) shows an absolute G magnitude versus $(G_{Bp}-G_{Rp})_0$ colour magnitude diagram for cluster members using distance $(M-m)_0^c$ and $E(B-V)^c$ from Tables 1 and 2.

(iv) Fig. 8(d) shows the 'Receiver Operator Characteristic' (ROC) curve for NGC 6705. This shows the true positive rate (TPR) versus the false positive rate (FPR) for increasing threshold probabilities of cluster membership. A random discriminator would have equal fractions of true and false positives for any probability threshold (shown as a dotted line in Fig. 4.4), whereas a perfect test would show a true positive rate of 1 above arbitrarily low probability thresholds. This provides a graphical illustration of the degree to which our calculated membership probabilities are an effective discriminator of cluster stars from field stars. ROC curves are shown for both P_{3D} and P_{2D} (see Section 3.4), although in the case of NGC 6705 the area under the ROC curve was almost identical. The results for P_{3D} are in general better and provide more discrimination than P_{2D} for more distant or sparsely populated clusters (see Section 5.2).

5 DISCUSSION

The main objective of this paper is to determine, on an individual basis, the probability that targets observed towards open and globular clusters as part of GES are members of that cluster. It is not intended, or possible, to provide a complete list of cluster members because the GES target sample was not spatially complete.

For most clusters the GES selected targets come from contiguous central areas of the clusters and will not have probed regions that are more distant from the centre. In addition, during the process of allocating targets to fibres in a discrete set of FLAMES fields, it is inevitable that there will be potential targets that could not be observed. On the other hand, the target selection was usually unbiased with respect to position in the CMD (between bright and faint limits of approximately $11 < V < 19$) by virtue of selecting targets from a CMD region that comfortably encompasses the likely locus of cluster members including equal-mass binary systems (Bragaglia et al., in preparation). The exceptions were (i) in almost all clusters, the relatively few UVES fibers in each field were preferentially allocated to (brighter) objects that had previous evidence of cluster membership; (ii) in the case of the globular clusters, both UVES and GIRAFFE fibers were preferentially allocated to targets with previous evidence for cluster membership.

Table 4. Results of the membership analysis for younger open clusters. Columns 2 to 7 show the mean and rms values of central velocity and intrinsic cluster dispersion used to determine the probability of cluster membership (see Section 4.2). Column 8 shows the fraction of the targets analysed that are expected cluster members. Columns 9 and 10 show the number of targets with membership probability $P_{3D} > 0.9$ and $P_{QG} > 0.9$, respectively.

Cluster	Cluster central velocity (km s^{-1})			Intrinsic dispersion of cluster (km s^{-1})			Fraction	Members $P > 0.9$	
	U_{RA}	U_{Dec}	U_{RV}	D_{RA}	D_{Dec}	D_{RV}	members	P_{3D}	P_{QG}
NGC 6530	8.48 ± 0.17	− 12.82 ± 0.12	0.15 ± 0.16	3.32 ± 0.15	2.23 ± 0.12	2.48 ± 0.16	0.34 ± 0.01	452	420
Trumpler 14	− 82.15 ± 0.26	29.71 ± 0.26	− 7.68 ± 0.55	4.38 ± 0.24	4.59 ± 0.21	8.08 ± 0.70	0.53 ± 0.02	320	302
Chamaeleon I	− 20.24 ± 0.10	0.35 ± 0.13	15.61 ± 0.14	0.91 ± 0.09	1.21 ± 0.09	0.90 ± 0.13	0.55 ± 0.04	90	62
Rho Ophiuchus	− 4.22 ± 0.12	− 17.20 ± 0.14	− 6.41 ± 0.30	0.76 ± 0.09	0.92 ± 0.10	1.36 ± 0.33	0.63 ± 0.06	45	39
NGC 2264	− 6.58 ± 0.08	− 12.64 ± 0.05	20.31 ± 0.13	1.64 ± 0.06	0.94 ± 0.04	2.39 ± 0.12	0.38 ± 0.01	502	424
NGC 2244	− 13.05 ± 0.14	1.05 ± 0.21	30.64 ± 0.29	1.25 ± 0.14	2.10 ± 0.20	2.47 ± 0.28	0.35 ± 0.03	120	110
Lambda Ori	1.98 ± 0.08	− 3.40 ± 0.11	26.80 ± 0.13	1.09 ± 0.07	1.47 ± 0.09	1.27 ± 0.12	0.60 ± 0.03	200	164
Lambda Ori B35	4.16 ± 0.16	− 4.60 ± 0.07	27.86 ± 0.19	1.11 ± 0.12	0.48 ± 0.06	0.79 ± 0.25	0.42 ± 0.05	49	38
25 Ori	2.24 ± 0.05	− 0.19 ± 0.06	20.65 ± 0.09	0.58 ± 0.04	0.75 ± 0.05	0.64 ± 0.09	0.68 ± 0.03	170	138
ASCC 50	− 25.04 ± 0.14	17.84 ± 0.12	21.70 ± 0.11	1.77 ± 0.16	1.52 ± 0.10	1.01 ± 0.13	0.41 ± 0.02	194	173
Collinder 197	− 26.47 ± 0.14	18.37 ± 0.17	20.82 ± 0.13	1.37 ± 0.12	1.63 ± 0.14	0.73 ± 0.15	0.37 ± 0.03	110	95
Gamma Velorum	− 10.65 ± 0.05	15.57 ± 0.09	18.24 ± 0.15	0.77 ± 0.05	1.31 ± 0.07	1.64 ± 0.15	0.45 ± 0.02	209	181
IC 4665	− 1.52 ± 0.08	− 13.92 ± 0.07	− 13.66 ± 0.14	0.41 ± 0.09	0.32 ± 0.10	0.22 ± 0.17	0.11 ± 0.02	33	29
NGC 2232	− 7.17 ± 0.04	− 2.63 ± 0.05	25.38 ± 0.09	0.35 ± 0.03	0.38 ± 0.04	0.18 ± 0.15	0.13 ± 0.01	82	78
NGC 2547	− 15.67 ± 0.04	7.88 ± 0.04	12.77 ± 0.08	0.50 ± 0.04	0.49 ± 0.04	0.54 ± 0.07	0.62 ± 0.03	165	138
IC 2602	− 12.68 ± 0.12	7.69 ± 0.12	17.61 ± 0.12	0.82 ± 0.11	0.82 ± 0.11	0.37 ± 0.22	0.53 ± 0.05	61	45
NGC 2451b	− 16.71 ± 0.12	8.24 ± 0.07	14.93 ± 0.12	0.95 ± 0.09	0.54 ± 0.06	0.44 ± 0.19	0.16 ± 0.02	63	51
NGC 6649	0.22 ± 0.28	− 1.42 ± 0.23	− 14.38 ± 1.11	1.96 ± 0.24	1.60 ± 0.22	6.46 ± 1.01	0.62 ± 0.05	65	64
IC 2391	− 17.70 ± 0.09	16.68 ± 0.09	14.80 ± 0.17	0.58 ± 0.06	0.58 ± 0.09	0.39 ± 0.25	0.61 ± 0.05	48	38
NGC 2451a	− 19.20 ± 0.17	13.88 ± 0.08	23.37 ± 0.09	1.07 ± 0.12	0.50 ± 0.07	0.16 ± 0.15	0.13 ± 0.02	40	33
NGC 6405	− 2.91 ± 0.09	− 12.91 ± 0.11	− 8.74 ± 0.14	0.71 ± 0.08	0.87 ± 0.09	0.71 ± 0.15	0.19 ± 0.02	60	54
NGC 6067	− 19.37 ± 0.10	− 25.71 ± 0.11	− 37.96 ± 0.23	1.27 ± 0.08	1.39 ± 0.09	1.84 ± 0.24	0.39 ± 0.02	181	179
NGC 2516	− 9.05 ± 0.04	21.92 ± 0.04	23.92 ± 0.05	0.87 ± 0.03	0.89 ± 0.03	0.75 ± 0.06	0.75 ± 0.02	476	420
Blanco 1	21.04 ± 0.05	2.96 ± 0.04	5.98 ± 0.07	0.48 ± 0.04	0.48 ± 0.05	0.23 ± 0.10	0.43 ± 0.03	128	123
NGC 6709	7.61 ± 0.08	− 18.27 ± 0.12	− 9.24 ± 0.13	0.61 ± 0.07	0.94 ± 0.09	0.54 ± 0.15	0.15 ± 0.01	71	64
NGC 6259	− 11.53 ± 0.16	− 31.66 ± 0.13	− 32.74 ± 0.41	1.74 ± 0.13	1.45 ± 0.11	3.26 ± 0.49	0.38 ± 0.03	136	125
NGC 6705	− 18.07 ± 0.08	− 48.80 ± 0.09	35.60 ± 0.15	1.74 ± 0.06	1.85 ± 0.06	2.20 ± 0.15	0.59 ± 0.02	559	526
Berkeley 30	− 4.26 ± 0.30	− 7.26 ± 0.37	47.71 ± 0.47	0.43 ± 0.38	1.13 ± 0.43	2.07 ± 0.64	0.34 ± 0.04	60	61
NGC 3532	− 23.61 ± 0.05	11.90 ± 0.05	5.46 ± 0.06	1.04 ± 0.04	1.02 ± 0.04	0.88 ± 0.05	0.73 ± 0.02	490	419
NGC 6281	− 4.60 ± 0.31	− 10.43 ± 0.16	− 4.41 ± 0.16	1.48 ± 0.27	0.73 ± 0.16	0.57 ± 0.16	0.44 ± 0.06	26	25
NGC 4815	− 99.15 ± 0.34	− 15.76 ± 0.28	− 27.35 ± 0.75	2.20 ± 0.29	1.61 ± 0.27	4.55 ± 0.66	0.50 ± 0.05	55	54
NGC 6633	2.13 ± 0.22	− 3.54 ± 0.19	− 28.16 ± 0.23	1.05 ± 0.18	0.89 ± 0.15	0.71 ± 0.28	0.21 ± 0.04	21	14

Table 3 provides the main catalogue of members with measured, GIRAFFE + HR15N and/or UVES spectra and Table A2 is a similar catalogue for supplementary target members observed with other GIRAFFE setups. These can be used to measure stellar properties and chemical abundances for a quantifiably reliable sample of cluster members. The accuracy of the discrimination achieved by the kinematic analyses was discussed in J20; tests made using independent membership criteria in young clusters showed that the derived membership probabilities give a reliable indication of both cluster membership and the residual contamination in any high probability sample of cluster members.

5.1 Selecting potential cluster members

Whilst the method used to assess membership probability was uniformly applied, the quantity and resolution of target data varies widely between clusters. This is best seen from the histograms in Appendix B indicating the number of potential cluster members, the level of contamination from likely background stars, and the scatter in velocities due to measurement uncertainties. These determine whether the maximum-likelihood analysis is able to resolve a group of member stars in velocity space that are distinct from the velocity distribution of the general background population. The criteria for success are that the plots in Appendix C of the three components of cluster central velocity U_i, and intrinsic dispersion D_i, show clearly defined peaks in log likelihood. If peaks are not found in one or more of U_i and D_i then the method breaks down and will identify increased numbers of false positives with incorrect membership probabilities.

The discrimination achieved by the maximum-likelihood analysis depends in part on the ratio of true cluster members to the numbers in the background population. For this reason, we filtered the initial target list to remove stars that are considered extremely unlikely to be cluster members by discarding background giants and/or distant background stars to produce the list of potential cluster members (see Section 3.1). This yielded satisfactory solutions for 67 of the 70 clusters – i.e. they show clear peaks in log likelihood for U_i and D_i. However 3 clusters initially failed to show a peak in one or more D_i components indicating further filtering was required.

For two clusters (ASCC 50 and NGC 6281) the criterion used to filter out distant background stars was tightened to reject stars with parallax smaller by at least 4σ than a value corresponding to $(M - m)_0^c + 1$ mag (compared to the standard criterion of $(M - m)_0^c + 2$ mag). This change produced the required peak in log likelihood of D_i for both clusters and relatively precise estimates of distance modulus (9.92 ± 0.06 and 8.62 ± 0.03, respectively), such that the margin of 1 mag used was still significantly above the required 4σ level.

Table 5. Results of the membership analysis for older open clusters and for globular clusters. Columns 2 to 7 show the mean and rms values of central velocity and intrinsic cluster dispersion used to determine the probability of cluster membership.(see Section 4.2). Column 8 shows the fraction of the targets analysed that are expected cluster members. Columns 9 and 10 show the number of targets with membership probability $P_{3D} > 0.9$ and $P_{QG} > 0.9$, respectively.

Cluster	Cluster central velocity (km s^{-1})			Intrinsic dispersion of cluster (km s^{-1})			Fraction	Members $P > 0.9$	
	U_{RA}	U_{Dec}	U_{RV}	D_{RA}	D_{Dec}	D_{RV}	members	P_{3D}	P_{QG}
Pismis 18	− 76.36 ± 0.18	− 30.46 ± 0.24	− 28.13 ± 0.47	0.72 ± 0.15	0.97 ± 0.21	1.23 ± 0.63	0.31 ± 0.05	23	23
Trumpler 23	− 55.29 ± 0.20	− 62.04 ± 0.23	− 61.48 ± 0.31	1.04 ± 0.20	1.30 ± 0.18	1.26 ± 0.35	0.47 ± 0.05	39	37
NGC 2355	− 34.21 ± 0.10	− 9.45 ± 0.10	36.37 ± 0.09	1.11 ± 0.08	1.08 ± 0.07	0.59 ± 0.09	0.69 ± 0.03	141	139
NGC 6802	− 40.13 ± 0.19	− 91.74 ± 0.22	13.47 ± 0.41	1.04 ± 0.17	1.27 ± 0.20	1.92 ± 0.45	0.56 ± 0.05	55	55
Ruprecht 134	− 19.39 ± 0.15	− 29.41 ± 0.19	− 40.53 ± 0.20	1.31 ± 0.21	1.71 ± 0.17	0.97 ± 0.28	0.18 ± 0.02	102	93
Berkeley 81	− 21.76 ± 0.28	− 35.99 ± 0.26	47.92 ± 0.22	0.70 ± 0.40	1.20 ± 0.34	0.69 ± 0.44	0.34 ± 0.04	56	56
NGC 6005	− 54.88 ± 0.21	− 51.34 ± 0.28	− 24.42 ± 0.22	1.12 ± 0.22	1.59 ± 0.32	1.04 ± 0.25	0.19 ± 0.02	55	51
Pismis 15	− 60.65 ± 0.22	38.68 ± 0.19	35.13 ± 0.16	1.03 ± 0.22	0.86 ± 0.19	0.46 ± 0.22	0.19 ± 0.03	36	36
Trumpler 20	-126.92 ± 0.13	2.97 ± 0.12	− 39.81 ± 0.14	1.43 ± 0.13	1.26 ± 0.13	1.29 ± 0.15	0.38 ± 0.02	172	167
Berkeley 44	− 0.54 ± 0.24	− 42.91 ± 0.18	− 8.54 ± 0.23	1.19 ± 0.24	0.75 ± 0.20	0.84 ± 0.26	0.51 ± 0.05	40	41
NGC 2141	− 1.91 ± 0.10	− 16.85 ± 0.09	26.39 ± 0.06	1.38 ± 0.10	1.48 ± 0.09	0.93 ± 0.07	0.76 ± 0.01	598	595
Czernik 24	5.03 ± 0.26	− 55.63 ± 0.20	22.22 ± 0.35	0.98 ± 0.31	1.02 ± 0.22	2.15 ± 0.39	0.27 ± 0.03	77	77
Haffner 10	− 22.73 ± 0.32	28.42 ± 0.33	88.00 ± 0.09	4.45 ± 0.33	4.65 ± 0.40	0.82 ± 0.10	0.62 ± 0.03	247	239
NGC 2158	− 3.98 ± 0.14	− 41.18 ± 0.12	28.68 ± 0.15	1.93 ± 0.14	1.75 ± 0.11	2.05 ± 0.14	0.67 ± 0.02	361	346
NGC 2420	− 14.81 ± 0.05	− 24.61 ± 0.06	74.62 ± 0.05	0.75 ± 0.05	0.92 ± 0.05	0.59 ± 0.05	0.75 ± 0.02	388	384
Berkeley 21	17.54 ± 0.32	− 35.10 ± 0.32	1.57 ± 0.38	0.81 ± 0.54	1.84 ± 0.48	2.67 ± 0.77	0.34 ± 0.02	178	178
Berkeley 73	7.13 ± 0.53	43.14 ± 0.54	97.33 ± 0.41	1.16 ± 0.74	0.92 ± 0.79	1.57 ± 0.51	0.66 ± 0.06	41	41
Berkeley 22	19.92 ± 0.42	− 13.04 ± 0.32	94.60 ± 0.19	1.87 ± 0.54	1.00 ± 0.50	1.12 ± 0.36	0.52 ± 0.03	170	170
Czernik 30	− 23.80 ± 0.35	− 2.91 ± 0.38	81.99 ± 0.15	1.20 ± 0.41	1.69 ± 0.44	0.58 ± 0.25	0.38 ± 0.04	69	69
Berkeley 31	5.29 ± 0.62	− 34.50 ± 0.52	56.97 ± 0.16	3.57 ± 1.39	3.68 ± 0.69	1.16 ± 0.22	0.34 ± 0.02	136	136
Berkeley 75	− 9.74 ± 0.31	47.97 ± 0.43	124.98 ± 0.13	0.36 ± 0.34	0.54 ± 0.49	0.21 ± 0.20	0.71 ± 0.06	43	43
Loden 165[a]	− 76.13 ± 0.70	34.09 ± 0.61	− 0.84 ± 2.06	3.00 ± 0.00	3.00 ± 0.00	16.68 ± 1.59	0.27 ± 0.03	77	70
NGC 6253	− 36.70 ± 0.09	− 42.71 ± 0.10	− 28.93 ± 0.11	1.05 ± 0.07	1.17 ± 0.09	0.90 ± 0.11	0.72 ± 0.03	162	154
Messier 67	− 44.77 ± 0.08	− 11.78 ± 0.08	34.00 ± 0.11	0.88 ± 0.06	0.85 ± 0.07	0.84 ± 0.12	0.92 ± 0.02	118	106
NGC 2425	− 58.42 ± 0.11	33.15 ± 0.12	103.68 ± 0.08	1.08 ± 0.10	1.15 ± 0.12	0.58 ± 0.09	0.31 ± 0.02	141	138
NGC 2243	− 27.19 ± 0.08	118.54 ± 0.09	59.79 ± 0.05	1.30 ± 0.08	1.23 ± 0.08	0.59 ± 0.07	0.88 ± 0.01	539	538
Berkeley 36	− 39.65 ± 0.16	21.98 ± 0.14	62.84 ± 0.12	1.20 ± 0.17	0.89 ± 0.16	1.17 ± 0.14	0.34 ± 0.02	212	212
Trumpler 5	− 9.71 ± 0.08	4.31 ± 0.08	51.60 ± 0.09	1.72 ± 0.08	1.61 ± 0.07	1.86 ± 0.09	0.76 ± 0.01	814	808
Berkeley 32	− 5.93 ± 0.14	− 26.58 ± 0.12	105.89 ± 0.07	1.42 ± 0.13	1.18 ± 0.10	0.60 ± 0.09	0.70 ± 0.03	240	238
Berkeley 39	− 37.29 ± 0.09	− 35.18 ± 0.08	58.85 ± 0.05	1.29 ± 0.10	1.22 ± 0.09	0.72 ± 0.06	0.62 ± 0.02	499	507
ESO 92-05	-231.28 ± 1.00	190.66 ± 0.98	61.47 ± 0.19	2.07 ± 1.56	2.70 ± 1.54	0.42 ± 0.41	0.80 ± 0.04	89	89
NGC 1261	208.60 ± 1.15	-268.51 ± 1.69	72.38 ± 0.44	7.85 ± 1.05	11.62 ± 1.68	3.01 ± 0.35	0.96 ± 0.02	63	59
NGC 362	375.88 ± 0.76	-142.68 ± 0.66	222.91 ± 0.47	7.72 ± 0.64	6.33 ± 0.56	4.14 ± 0.41	0.88 ± 0.04	104	91
NGC 2808	56.73 ± 0.75	15.98 ± 0.94	103.66 ± 0.76	7.84 ± 0.61	9.42 ± 0.88	7.22 ± 0.58	0.73 ± 0.04	112	122
NGC 1904	194.63 ± 0.90	− 127.13 ± 0.89	205.85 ± 0.40	6.64 ± 0.68	6.37 ± 0.72	2.58 ± 0.34	0.94 ± 0.03	59	58
NGC 6752	− 68.96 ± 0.37	− 86.93 ± 0.36	− 26.13 ± 0.32	5.98 ± 0.28	5.92 ± 0.27	4.49 ± 0.24	0.96 ± 0.01	284	238
NGC 5927	-287.38 ± 1.05	− 180.65 ± 0.96	− 103.29 ± 0.53	8.74 ± 0.89	7.82 ± 0.75	4.13 ± 0.40	0.89 ± 0.03	80	71
NGC 104	120.10 ± 0.61	− 59.03 ± 0.62	− 18.07 ± 0.51	10.36 ± 0.47	10.46 ± 0.50	7.49 ± 0.38	0.98 ± 0.01	286	255

Note. [a]Components of the intrinsic cluster dispersion are artificially constrained in maximum-likelihood fit for Loden 165 (see Section 5.1).

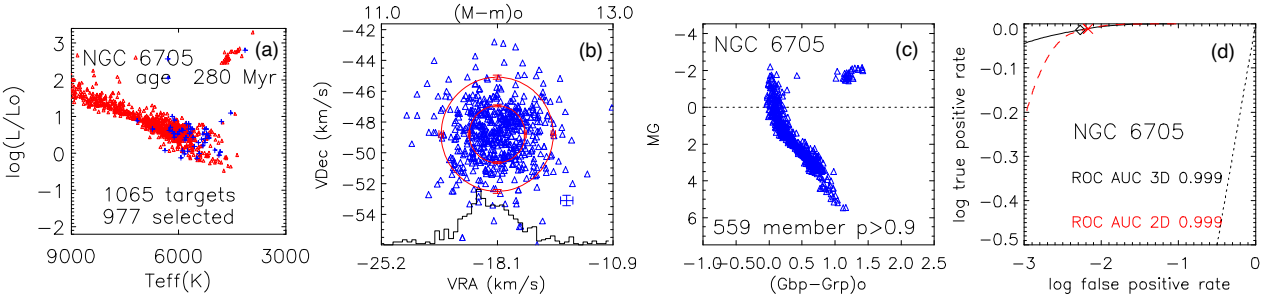

Figure 8. Plots of potential and likely cluster members of NGC 6705. (a) The HR diagram of valid targets observed in the cluster with stars identified as likely background giants shown as blue crosses. (b) Tangential velocities, V_{Dec} versus V_{RA} for likely ($P_{3D} > 0.9$) cluster members where the cross indicates the median measurement uncertainty and the ellipses show one and two times the cluster intrinsic dispersion. The black line on this plot shows a histogram of the relative number of members versus parallax (see scale above the plot). (c) *Gaia* absolute G magnitude versus $(G_{BP} - G_{RP})_0$ for $P_{3D} > 0.9$ members. (d) The Receiver Operator Characteristic curves for P_{3D} and P_{2D} membership data (solid black and dashed red curves, respectively). 90 per cent probability values are marked on the curve by a black diamond and red cross. The dotted line shows the ROC expected for randomly partitioned data.

Loden 165 however, is a poorly defined cluster with no identifiable peak in the *RV* histogram (see Appendix B). A solution was computed by capping the intrinsic dispersions, $D_{\rm RA}$ and $D_{\rm Dec}$ at a maximum value of 3.0 km s^{-1}. This produced a false solution, the results of which are shown graphically in Appendix D. From the CMD it can be seen that high probability ($P_{\rm 3D} > 0.9$) cluster members do not fall around a common isochrone suggesting the sample includes an excess numbers of false positives. No satisfactory solution was found for Loden 165, hence no membership probabilities are reported in Table 3.

5.2 The effects of selection criteria on discrimination

Fig. 9 summarizes the area under the curve (AUC, also known as the c-statistic) of the ROC for each cluster in age order (excluding Loden 165). The AUC is equivalent to the probability that our classification will give a randomly chosen member a higher probability of membership than a randomly chosen non-member and can be used as a figure of merit for judging how successful a binary classifier is at discriminating between the two possibilities (e.g. Hosmer & Lemeshow 2000). The discrimination achieved between members and background targets depends on the data available for a particular cluster and the method of analysis. In this paper, we report results of 3D analyses, $P_{\rm 3D}$ using both proper motion and *RV* data, which always provide better discrimination than a 2D analysis of proper motion data alone, $P_{\rm 2D}$.

Fig. 9 compares the AUC for both 2D and 3D analyses. For about half of the clusters – those that are nearby and hence have cluster members that form a distinct and narrow peak in proper motion space – the 2D membership AUC is already very high (> 0.99) and the addition of the third dimension of *RV* makes only a small improvement to the AUC. However for many of the remaining clusters, particularly those that are more distant or for which the proper motion coincides with the peak of the proper motion of field stars, the use of *RV* data improves the AUC, and hence the level of discrimination, significantly. In fact, for five open clusters (ASCC 50, NGC 6005, Haffner 10, Berkeley 21, and Berkeley 31), the 2D analysis failed to converge at all. i.e. A 3D analysis was mandatory to kinematically identify cluster members.

The seven globular clusters (at the bottom of Fig. 9) have lower AUC values than most of the open clusters. This is the result of the target selection process rather than any difference in cluster kinematics or the method of analysis. For the open clusters ∼50 per cent or more of the targets are likely background stars with $P_{\rm 3D} < 0.1$. Thus the distribution of background stars is well defined by the maximum-likelihood analysis allowing members of well populated clusters to be discriminated for the background population. In contrast, for the the globular clusters, the target samples were already pre-selected to be likely cluster members; they contain, on average, only 5 per cent of probable background stars. This amounts to only a few measured stars which is insufficient to fully characterize background populations that are well separated from the distribution of cluster members in velocity space (see Appendix B). For these clusters it is not possible to clearly identify non-members. Instead, individual $P_{\rm 3D}$ values must be used to assess the probability that outliers in kinematic space are cluster members.

Membership probabilities were also calculated for a restricted list of targets that was filtered to remove those with potentially problematic *Gaia* data (see Section 3.2). The membership probabilities in this case are referred to as $P_{\rm QG}$. For individual stars present in both lists $P_{\rm 3D}$ and $P_{\rm QG}$ are almost always very similar: <1 per cent of targets have a difference $|\Delta P| > 0.01$. Filtering targets with suspect *Gaia*

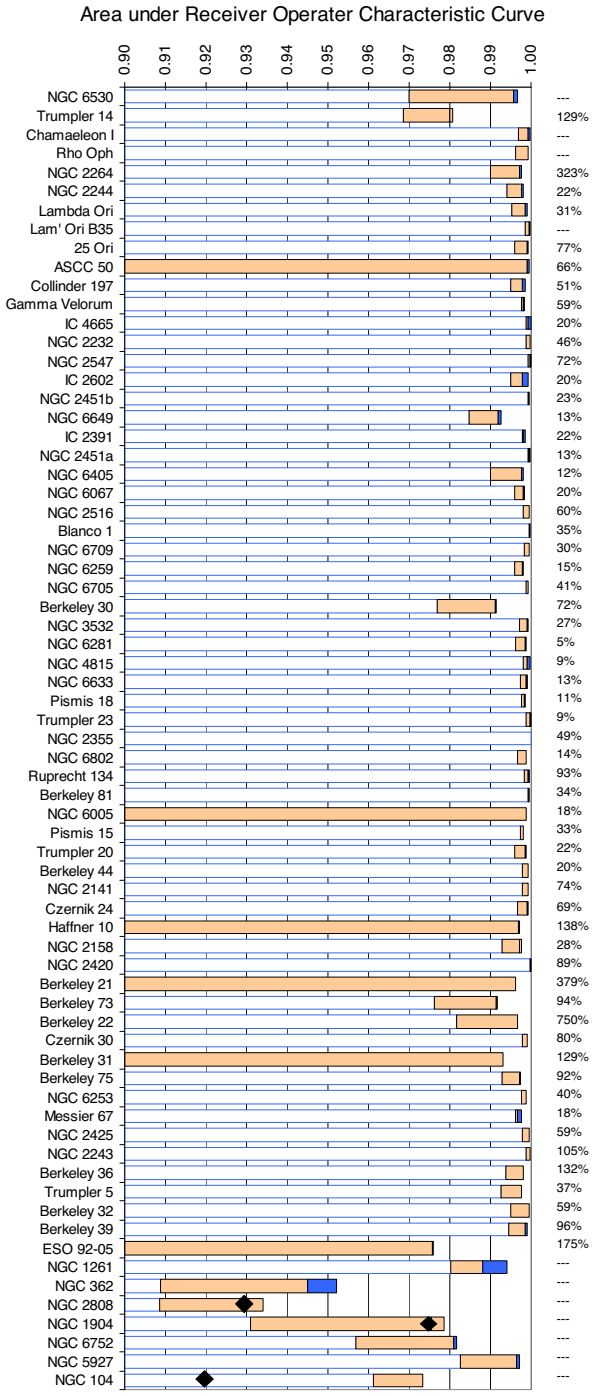

Figure 9. Stacked bar chart showing the area under the Receiver Operator Characteristic curves (ROC AUC) shown in Appendix C for *Gaia*–ESO clusters. The right edge of the unfilled bar indicates the ROC AUC for $P_{\rm 2D}$ data, the right edge of the light brown bar shows the ROC 'area under the curve' (AUC) statistic for $P_{\rm 3D}$. The right edge of the blue bar gives the ROC AUC for based on $P_{\rm QG}$, as defined in Section 5.2, Where the AUC is lower than derived from $P_{\rm 3D}$ its value is marked with a diamond. Percentages on the right-hand side of the plot show the ratio of the number *Gaia*–ESO cluster members compared to the number identified purely from *Gaia* DR2 data by Cantat-Gaudin et al. (2018) (see Section 5.4).

data also has little effect on discrimination. For the open clusters it produced either no change or a marginal increase (<0.2 per cent) in AUC. Globular clusters, which contain a higher proportion of targets with suspect *Gaia* data and small numbers of non-members, show larger changes in AUC, both positive and negative (see Fig. 9). For most applications P_{3D} is preferred since it identifies about 7 per cent more $P > 0.9$ cluster members and any target selected as a likely member on the basis of its kinematic properties almost certainly has good proper motion data (see J20 for a detailed discussion). However, for particular applications the reader may wish to avoid stars with suspect *Gaia* data in which case P_{QG} is available in Table 3.

5.3 Comparison with previous kinematic analysis

J20 reported membership probabilities for 32 open clusters using GESiDR5 data cross-matched with *Gaia* DR2. The method of kinematic analysis used here is similar to that used in J20 although the method of selecting potential cluster members has been updated to reflect the greater mix of cluster ages and distances in GESiDR6 data. We compare results between J20 and the present analysis by counting the number of targets that are identified as cluster members $P_{3D} > 0.9$ in the present analysis but have a membership probability $P_{3D} < 0.8$ in the J20 analysis. There are a total of 288 GES targets in the 32 clusters that show this change in membership probability. Of these, 121 are targets with the same *Gaia* source ID in both analyses with the remainder showing different *Gaia* source IDs.

NGC 6530 has 29 new members compared with the J20 analysis (and with the same *Gaia* counterpart) and shows a significant improvement in the quality of fit of the model distribution to the measured V_{RA} data (See Appendix B and the equivalent plot in J20) due, most probably, to the increase in the number of targets selected as potential cluster members. In J20, targets with no GES T_{eff} were excluded from the analysis whereas in the current analysis T_{eff}^{p} is estimated where no GES value is available (see Section 2.5). Other clusters show smaller numbers of mismatched membership for targets with the same *Gaia* source ID, most of which are associated with relatively large changes ($>3\sigma$) in proper motion between *Gaia* DR2 and EDR3. For example NGC 2264 has 14 new members, 12 with a $>3\sigma$ change in proper motion.

There are 167 targets that are newly assigned membership in this paper but have different *Gaia* source IDs in J20. In J20 GES targets were identified with the nearest source in the 2MASS catalogue. In this paper, we adopt the *Gaia* ID given in the GESiDR6 catalogue (see Hourihane et al., in preparation). This provides a better, but still not a perfect, cross-match to *Gaia* source IDs for a target list that includes non-2MASS sources in several of the more distant clusters. Any mismatched targets are unlikely to have been ascribed cluster membership so this difficulty is a source of incompleteness rather than contamination.

5.4 Comparison with other work

Cantat-Gaudin et al. (2018) applied an unsupervised membership assignment algorithm to *Gaia* DR2 data to characterize Milky Way star clusters, producing membership lists and cluster parameters for 1229 clusters. Cross-referencing target RA and Dec in Table 3 with the results of Cantat-Gaudin et al. identified matches for 58 of the 63 open clusters considered in this paper; the exceptions are the young clusters Chamaeleon I, Lambda Ori B35, NGC 6530 and Rho Ophiuchus, and Loden 165 (where we have no membership data). For each cluster we compare the number of stars with membership probability $P_{CG} \geq 0.5$ in Table 1 of Cantat-Gaudin et al. (2018) with

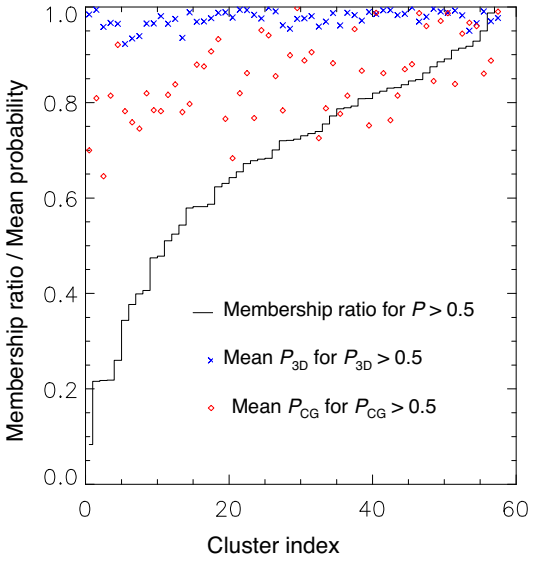

Figure 10. Comparison of cluster membership for targets in Table 3 of this paper with results reported in Cantat-Gaudin et al. (2018) for 58 open clusters common to both data sets. Clusters are ordered by increasing ratio of common targets identified as likely cluster members ($P_{3D} > 0.5$) in Cantat-Gaudin et al. to those identified in this paper (see Section 5.4), which is shown as a black line. The blue and red points are the average membership probability for targets with $P > 0.5$ in each cluster from this paper and from Cantat-Gaudin et al., respectively.

the number of $P_{3D} \geq 0.5$ targets in Table 3; the ratio giving a rough indication of the relative completeness of our list of GES+EDR3 cluster members compared to a membership list derived solely from *Gaia* DR2 data. Results for each cluster are shown on the RHS of the plot in in Fig. 9. The median value over the 58 matched clusters is 40 per cent. i.e. Cantat-Gaudin et al. have identified more stars as members. However within this number there are significant variations according to cluster age and distance. The analysis based solely on *Gaia* DR2 data fails to identify any members in 3 of the 6 youngest clusters (aged <4 Myr in Table 1) and in two other cases, Trumpler 14 and NGC 2264, Cantat-Gaudin et al. report fewer members than are identified here. The median ratio increases to 70 per cent for more distant clusters (>2 kpc) nine of which show higher numbers of targets identified from the *Gaia*-ESO data.

Next we compare the number of targets common to both data sets that are likely cluster members: with $P \geq 0.5$ in both data sets. However, the values specific to each cluster vary a lot. The results are shown in Fig. 10 as a solid line, with the clusters ordered by increasing values of the membership ratio. The clusters where the ratio is <0.5 tend to be the more distant clusters where the addition of *RV* data becomes more important and where clusters tend to be projected against higher levels of field star contamination. Also shown in Fig. 10 are the average values of membership probability for likely cluster members (those with $P_{3D} > 0.5$ or $P_{CG} > 0.5$) from Table 3 and from Cantat-Gaudin et al. (2018). The mean values of membership probability for these samples across all clusters is 98 per cent for the data in Table 3 compared to 85 per cent for data from Cantat-Gaudin et al. indicating that the number of false positives (i.e. the level of contamination expected) is, on average, 6 times lower using Table 3. This ratio turns out to be quite independent of the chosen cut-off level used to define likely cluster members.

The differing numbers of members and levels of discrimination between these two data sets likely reflects how samples of poten-

tial cluster members were selected for analysis and the available kinematic data. Cantat-Gaudin et al. (2018) placed no restrictions on potential targets, apart from a cut off in G magnitude for their analysis of *Gaia* astrometric data. For many clusters the sky positions of the Cantat-Gaudin et al. members extend well beyond the confines of the GES survey, particularly for nearby clusters. Conversely the analysis reported here considers a restricted list of potential cluster members selected as targets for GES observations with some further screening to remove targets considered highly unlikely to be cluster members (see Section 3.1). This selection process together with use of GES *RV* data alongside improved *Gaia* EDR3 astrometric data achieves a higher level of discrimination and much lower fraction of false positives, albeit from a smaller parent sample.

6 SUMMARY

As a part of the *Gaia*–ESO survey (GES) 39 441 targets towards 63 open clusters and 7 globular clusters were observed using the GIRAFFE medium resolution spectrograph (with the HR15N setup) and/or the UVES high resolution spectrograph. Parameters from these spectra, reported in the final GES data release, have been combined with *Gaia* EDR3, 2MASS, and VISTA data to determine the probability of individual targets being cluster members.

After an initial filtering process, a maximum-likelihood technique was used to determine membership probabilities for each of these stars based solely on their 3D kinematics. Reliable solutions were obtained for 69 of the 70 clusters with a high discrimination achieved between members and non-members of the individual clusters: the areas under their Receiver Operator Characteristic curves are $\geq$0.975 for all open clusters. Of the potential cluster members that go into the kinematic analysis for 69 clusters, 47 per cent were identified as likely members with an average probability of $P_{3D} = 0.993$, 48 per cent were flagged as non-members with an average of $P_{3D} < 0.005$, and only 5 per cent were of uncertain status ($0.1 < P_{3D} < 0.9$). The inclusion of the GES spectroscopic data and radial velocities is of significant benefit to membership discrimination and especially in the reduction of false positives. This is particularly apparent in more distant clusters and those with significant contamination in the proper motion plane by field stars.

Results are presented in the form of a main catalogue of compiled data that includes the membership probability for 26351 potential cluster members observed using GIRAFFE + HR15N setup and/or UVES. Membership probabilities are shown for two cases: P_{3D} calculated for the full list of potential cluster members; and P_{QG} calculated for a restricted list filtered to remove ∼9 per cent of targets with potentially suspect *Gaia* data. Membership probabilities are also given for a further 3193 potential cluster members that were observed using alternate GIRAFFE setups and were excluded from the main kinematic analysis.

Since the membership criteria are almost purely kinematic, and independent of stellar photometry and chemistry, then the union of this catalogue with GES, *Gaia* EDR3, or other data sets is ideal for studying the behaviour of photometric, chemical, or other physical properties as a function of mass, age, or Galactic position, without compromising investigations by using those same properties as membership criteria. Examples include testing stellar evolutionary models using HR and colour–magnitude diagrams (e.g. Randich et al. 2018). following the evolution of magnetic activity, rotation, and light element depletion (e.g. Jeffries et al. 2017; Gutiérrez Albarrán et al. 2020), studying chemical inhomogeneity within clusters (e.g. Spina et al. 2015, 2018) or investigating chemical abundance gradients with age and Galactocentric radius (e.g. Spina et al. 2017; Magrini et al. 2018).

ACKNOWLEDGEMENTS

RJJ, RDJ, and NJW wish to thank the UK Science and Technology Facilities Council for financial support.

Based on data products from observations made with ESO Telescopes at the La Silla Paranal Observatory under programme ID 188.B-3002. These data products have been processed by the Cambridge Astronomy Survey Unit (CASU) at the Institute of Astronomy, University of Cambridge, and by the FLAMES/UVES reduction team at INAF/Osservatorio Astrofisico di Arcetri. These data have been obtained from the *Gaia*–ESO Survey Data Archive, prepared and hosted by the Wide Field Astronomy Unit, Institute for Astronomy, University of Edinburgh, which is funded by the UK Science and Technology Facilities Council. This work was partly supported by the European Union FP7 programme through ERC grant number 320360 and by the Leverhulme Trust through grant RPG-2012-541. We acknowledge the support from INAF and Ministero dell' Istruzione, dell' Università' e della Ricerca (MIUR) in the form of the grant 'Premiale VLT 2012". TB was funded by grant No. 2018-04857 from The Swedish Research Council. The results presented here benefit from discussions held during the *Gaia*–ESO workshops and conferences supported by the ESF (European Science Foundation) through the GREAT Research Network Programme.

This work has made use of data from the European Space Agency (ESA) mission *Gaia* (https://www.cosmos.esa.int/gaia), processed by the *Gaia* Data Processing and Analysis Consortium (DPAC, https://www.cosmos.esa.int/web/gaia/dpac/consortium). Funding for the DPAC has been provided by national institutions, in particular the institutions participating in the *Gaia* Multilateral Agreement.

This paper also uses data products from: the VISTA Hemisphere Survey, ESO programme ID: 179.A-2010; the VISTA Variables in the Via Lactea Survey, ESO programme ID: 179.B-2002 and the Two Micron All Sky Survey, which is a joint project of the University of Massachusetts and the Infrared Processing and Analysis Center/California Institute of Technology, funded by the National Aeronautics and Space Administration and the National Science Foundation.

DATA AVAILABILITY STATEMENT

The reduced stacked spectra underlying this article can be obtained via the European Southern Observatory (ESO) archive and is identified as the 'Phase 3 release' of Gaia–ESO Survey DR4. Raw data can also be obtained from the ESO archive. The full catalogue of stellar parameters derived from these spectra by the various GES working groups will be deposited in this same archive shortly. All the other data used in this paper (*Gaia*, 2MASS, VISTA) are also available in public archives.

REFERENCES

Anthony-Twarog B. J., Atwell J., Twarog B. A., 2005, AJ, 129, 872
Anthony-Twarog B. J., Tanner D., Cracraft M., Twarog B. A., 2006, AJ, 131, 461
Arenou F. et al., 2018, A&A, 616, A17
Binks A. S. et al., 2021, MNRAS, 505, 1280
Bonatto C., Bica E., 2007, MNRAS, 377, 1301
Bragaglia A., Tessicini G., Tosi M., Marconi G., Munari U., 1997, MNRAS, 284, 477

Busso G. et al., 2018, Gaia Data Processing and Analysis Consortium, Gaia DR2 documentation European Space Agency. Chapter 5: Photometry. Available at: https://gea.esac.esa.int/archive/documentation/GDR2/
Cantat-Gaudin T. et al., 2014, A&A, 569, A17
Cantat-Gaudin T. et al., 2018, A&A, 618, A93
Cargile P. A., James D. J., Jeffries R. D., 2010, ApJ, 725, L111
Carraro G., Ortolani S., 1994, A&AS, 106, 573
Carraro G., Patat F., Baumgardt H., 2001, A&A, 371, 107
Carraro G., Girardi L., Marigo P., 2002, MNRAS, 332, 705
Carraro G., Geisler D., Baume G., Vázquez R., Moitinho A., 2005, MNRAS, 360, 655
Carraro G., Janes K. A., Costa E., Méndez R. A., 2006, MNRAS, 368, 1078
Carraro G., Costa E., Ahumada J. A., 2010, AJ, 140, 954
Carretta E., Gratton R. G., Clementini G., Fusi Pecci F., 2000, ApJ, 533, 215
Casagrande L., VandenBerg D. A., 2018, MNRAS, 479, L102
Chen L., de Grijs R., Zhao J. L., 2007, AJ, 134, 1368
Chen B. Q. et al., 2019, MNRAS, 483, 4277
Ciechanowska A., Pietrzynski G., Wyrzykowski L., Szewczyk O., Kubiak M., Udalski A., Szymanski M. K., 2006, Acta Astron., 56, 219
Cignoni M., Beccari G., Bragaglia A., Tosi M., 2011, MNRAS, 416, 1077
Clem J. L., Landolt A. U., Hoard D. W., Wachter S., 2011, AJ, 141, 115
Cottaar M., Meyer M. R., Parker R. J., 2012, A&A, 547, A35
Damiani F. et al., 2014, A&A, 566, A50
Dekker H., D'Odorico S., Kaufer A., Delabre B., Kotzlowski H., 2000, in Iye M., Moorwood A. F., eds, Proc. SPIE Conf. Ser. Vol. 4008, Design, construction, and performance of UVES, the echelle spectrograph for the UT2 Kueyen Telescope at the ESO Paranal Observatory. SPIE, Bellingham, p. 534
Di Fabrizio L., Bragaglia A., Tosi M., Marconi G., 2005, MNRAS, 359, 966
Dias W. S., Alessi B. S., Moitinho A., Lépine J. R. D., 2002, A&A, 389, 871
Diplas A., Savage B. D., 1994, ApJS, 93, 211
Dolan C. J., Mathieu R. D., 1999, AJ, 118, 2409
Dolan C. J., Mathieu R. D., 2002, AJ, 123, 387
Donati P., Beccari G., Bragaglia A., Cignoni M., Tosi M., 2014, MNRAS, 437, 1241
Donati P., Bragaglia A., Carretta E., D'Orazi V., Tosi M., Cusano F., Carini R., 2015, MNRAS, 453, 4185
Downes J. J. et al., 2014, MNRAS, 444, 1793
Erickson K. L., Wilking B. A., Meyer M. R., Robinson J. G., Stephenson L. N., 2011, AJ, 142, 140
Forbes D. A., Bridges T., 2010, MNRAS, 404, 1203
Friel E. D., Jacobson H. R., Pilachowski C. A., 2010, AJ, 139, 1942
Friel E. D. et al., 2014, A&A, 563, A117
Froebrich D., Schmeja S., Samuel D., Lucas P. W., 2010, MNRAS, 409, 1281
Gaia Collaboration 2016, A&A, 595, A2
Gaia Collaboration 2018, A&A, 616, A1
Gilmore G. et al., 2012, Messenger, 147, 25
Gutiérrez Albarrán M. L. et al., 2020, A&A, 643, A71
Harris W. E., 1996, AJ, 112, 1487
Hasegawa T., Sakamoto T., Malasan H. L., 2008, PASJ, 60, 1267
Hatzidimitriou D. et al., 2019, A&A, 626, A90
Hayes C. R., Friel E. D., Slack T. J., Boberg O. M., 2015, AJ, 150, 200
Hill G., Perry C. L., 1969, AJ, 74, 1011
Hosmer D. W., Lemeshow S., 2000, Applied Logistic Regression, 2nd edn.Vol. 350. John Wiley & Sons, New York
Hünsch M., Weidner C., 2003, in Brown A., Harper G. M., Ayres T. R., eds, Cambridge Workshop on Cool Stars, Stellar Systems, and the Sun, Vol. 12, The Future of Cool-Star Astrophysics: 12th Cambridge Workshop on Cool Stars, Stellar Systems, and the Sun. University of Colorado, Boulder, CO, p. 787
Hur H., Sung H., Bessell M. S., 2012, AJ, 143, 41
Jackson R. J. et al., 2015, A&A, 580, A75
Jackson R. J. et al., 2020, MNRAS, 496, 4701 (J20)
Jacobson H. R. et al., 2016, A&A, 591, A37
Janes K. A., Hoq S., 2011, AJ, 141, 92
Jeffries R. D., Jackson R. J., James D. J., Cargile P. A., 2009, MNRAS, 400, 317
Jeffries R. D. et al., 2014, A&A, 563, A94
Jeffries R. D. et al., 2017, MNRAS, 464, 1456
Kassis M., Janes K. A., Friel E. D., Phelps R. L., 1997, AJ, 113, 1723
Kharchenko N. V., Piskunov A. E., Schilbach E., Röser S., Scholz R.-D., 2013, A&A, 558, A53
Kılıçoğlu T., Monier R., Richer J., Fossati L., Albayrak B., 2016, AJ, 151, 49
Kim S. C. et al., 2005, J. Korean Astron. Soc., 38, 429
Kuhn M. A., Hillenbrand L. A., Sills A., Feigelson E. D., Getman K. V., 2019, ApJ, 870, 32
Lindegren L. et al., 2018, A&A, 616, A2
Lindegren L. et al., 2021, A&A, 649, A2
Loinard L., Torres R. M., Mioduszewski A. J., Rodríguez L. F., 2008, ApJ, 675, L29
Luhman K. L., 2007, ApJS, 173, 104
Lyra W., Moitinho A., van der Bliek N. S., Alves J., 2006, A&A, 453, 101
Madore B. F., van den Bergh S., 1975, ApJ, 197, 55
Magrini L. et al., 2015, A&A, 580, A85
Magrini L. et al., 2018, A&A, 617, A106
McMahon R. G., Banerji M., Gonzalez E., Koposov S. E., Bejar V. J., Lodieu N., Rebolo R., VHS Collaboration, 2013, Messenger, 154, 35
Mermilliod J.-C., Clariá J. J., Andersen J., Piatti A. E., Mayor M., 2001, A&A, 375, 30
Minniti D. et al., 2010, New Astron., 15, 433
Moraux E., Bouvier J., Stauffer J. R., Barrado y Navascués D., Cuillandre J.-C., 2007, A&A, 471, 499
Naylor T., Jeffries R. D., 2006, MNRAS, 373, 1251
Ortolani S., Bica E., Barbuy B., Zoccali M., 2005, A&A, 429, 607
Ortolani S., Bica E., Barbuy B., 2008, MNRAS, 388, 723
Overbeek J. C. et al., 2017, A&A, 598, A68
Pancino E. et al., 2017, A&A, 598, A5
Pasquini L. et al., 2002, Messenger, 110, 1
Piatti A. E., Clariá J. J., Bica E., Geisler D., Minniti D., 1998, AJ, 116, 801
Piatti A. E., Clariá J. J., Ahumada A. V., 2004, MNRAS, 349, 641
Platais I., Kozhurina-Platais V., Barnes S., Girard T. M., Demarque P., van Altena W. F., Deliyannis C. P., Horch E., 2001, AJ, 122, 1486
Prisinzano L., Damiani F., Micela G., Sciortino S., 2005, A&A, 430, 941
Prisinzano L., Damiani F., Guarcello M. G., Micela G., Sciortino S., Tognelli E., Venuti L., 2018, A&A, 617, A63
Prisinzano L. et al., 2019, A&A, 623, A159
Pryor C., Meylan G., 1993, in Djorgovski S. G., Meylan G., eds, ASP Conf. Ser. Vol. 50, Velocity Dispersions for Galactic Globular Clusters. Astron. Soc.Pac., San Francisco, p. 357
Raghavan D. et al., 2010, ApJS, 190, 1
Randich S., Gilmore G., Gaia-ESO Consortium, 2013, Messenger, 154, 47
Randich S. et al., 2018, A&A, 612, A99
Sacco G. G. et al., 2014, A&A, 565, A113
Sacco G. G. et al., 2015, A&A, 574, L7
Sagar R., Griffiths W. K., 1998, MNRAS, 299, 1
Salaris M., Weiss A., Percival S. M., 2004, A&A, 414, 163
Santos J. F. C., Bonatto C., Bica E., 2005, A&A, 442, 201
Sharma S., Pandey A. K., Ogura K., Mito H., Tarusawa K., Sagar R., 2006, AJ, 132, 1669
Skrutskie M. F. et al., 2006, AJ, 131, 1163
Spina L. et al., 2015, A&A, 582, L6
Spina L. et al., 2017, A&A, 601, A70
Spina L., Meléndez J., Casey A. R., Karakas A. I., Tucci-Maia M., 2018, ApJ, 863, 179
Suárez G. et al., 2017, AJ, 154, 14
Sung H., Bessell M. S., Lee S.-W., 1997, AJ, 114, 2644
Sung H., Chun M.-Y., Bessell M. S., 2000, AJ, 120, 333
Sung H., Bessell M. S., Lee B.-W., Lee S.-G., 2002, AJ, 123, 290
Tang B. et al., 2017, A&A, 601, A56
Tognelli E., Prada Moroni P. G., Degl'Innocenti S., 2011, A&A, 533, A109
Tosi M., Bragaglia A., Cignoni M., 2007, MNRAS, 378, 730
Turner D. G., 2012, Astron. Nachr., 333, 174
van Leeuwen F., 2009, A&A, 497, 209
Venuti L. et al., 2018, A&A, 609, A10
Walker A. R., Laney C. D., 1987, MNRAS, 224, 61

Whittet D. C. B., Prusti T., Franco G. A. P., Gerakines P. A., Kilkenny D., Larson K. A., Wesselius P. R., 1997, A&A, 327, 1194
Yong D., Carney B. W., Friel E. D., 2012, AJ, 144, 95
Yuan H. B., Liu X. W., Xiang M. S., 2013, MNRAS, 430, 2188

SUPPORTING INFORMATION

Supplementary data are available at *MNRAS* online.

Appendix B. Measured Data and Model Fits.
Appendix C. Cluster Velocity and Dispersion.
Appendix D. Plots of Cluster Members.
Table 3. Membership probabilities for GESiDR6 cluster targets.
Table A2. Membership probabilities of supplementary targets.

Please note: Oxford University Press is not responsible for the content or functionality of any supporting materials supplied by the authors. Any queries (other than missing material) should be directed to the corresponding author for the article.

APPENDIX A: SUPPLEMENTARY TARGETS

In this section, we evaluate the membership probability of supplementary targets observed towards the clusters listed in Tables 1 and 2 using alternative GIRAFFE setups. These are targets with a measured *RV* reported in the GESiDR6 Parameter Catalogue but which were not observed with the GIRAFFE HR15N setup or with UVES. These targets could not pass through all the same filtering steps described in Section 3.1 since they did not have the γ and τ spectroscopic indices. A total of 3770 additional targets were identified in 30 clusters, the remaining 40 clusters showed no additional targets. Selection criteria for these additional targets was varied. In some cases targets were chosen on the same basis as GIRAFFE + HR15N targets but in other clusters the targets had previous evidence of cluster membership. It is for these reasons that we chose to treat these targets separately and the membership probabilities may be less accurate than for the main sample.

Potential cluster members had their luminosity and mass estimated as in Section 3.3, the only difference in the target data being the source of the measured *RV* and its uncertainty. For the main kinematic analyses, the *RV* of targets observed using GIRAFFE was taken from the spectrum VELCLASS metadata and its uncertainty estimated from an empirical analysis of repeat observations (see Section 2.3). For these additional targets the measured *RV* and uncertainty were taken from the GESiDR6 Parameter Catalogue in which the reported *RV* was averaged over observations made using a variety of GIRAFFE setups. A small (0.09 km s^{-1}) correction was added to the catalogue *RV* to match the GIRAFFE HR15N *RV* scale.

Membership probabilities for these additional targets were calculated as the expectation value of being a cluster member evaluated over the grid of model velocities, dispersions, and fractional membership weighted according to the total likelihood summed over potential cluster members that were observed with Giraffe+HR15N and/or UVES – thus giving the probability that an additional target is a member of the cluster as defined by main GIRAFFE + HR15N and UVES data set.

This approach is considered more robust to systematic differences in the *RV* measured using different GIRAFFE setups and/or variations in the method of target selection. Any systematic offset in *RV* for an individual target will tend to reduce P_{3D}. Similarly if an additional target is selected from a data set previously identified as cluster members then P_{3D} should give a conservative estimate of membership probability based on the kinematics of the Giraffe + HR15N and UVES stars. These additional targets thus have no effect on the best-fitting cluster parameters in Tables 4 and 5.

Table A1 shows the numbers of supplementary targets, potential cluster members, and $P_{3D} > 0.9$ cluster members in each cluster. There are a total of 1875 additional $P_{3D} > 0.9$ cluster members, 911 in open clusters and 964 in globular clusters. Membership probabilities for individual additional targets are given in Table A2.

Table A1. Numbers of supplementary targets with *RV* reported in the GESiDR6 Parameter Catalogue that were *not* observed with the GIRAFFE HR15N setup or with UVES.

Cluster	Number of targets	Number fitted	Members $P_{3D} > 0.9$
Trumpler 14	41	24	10
NGC 2232	61	25	0
NGC 6649	25	22	11
NGC 6405	38	33	20
NGC 6067	82	59	29
NGC 6709	46	45	13
NGC 6259	28	23	6
NGC 6705	11	10	9
Berkeley 30	55	34	11
NGC 3532	172	148	122
NGC 6281	69	49	30
NGC 4815	50	45	23
NGC 6633	68	20	8
Pismis 18	34	30	10
Trumpler 23	59	54	27
NGC 6802	47	46	39
Berkeley 81	64	44	9
NGC 6005	198	171	44
Pismis 15	92	83	25
Trumpler 20	699	645	296
Haffner 10	76	53	7
NGC 6253	352	309	115
NGC 2243	6	6	6
Berkeley 32	49	47	41
NGC 1261	179	144	126
NGC 362	255	210	133
NGC 2808	144	113	56
NGC 1904	154	115	85
NGC 6752	353	335	322
NGC 104	263	251	242

Table A2. Membership probabilities of supplementary targets. Columns 1 to 4 show GESiDR6 target name, cluster, and co-ordinates. Targets flagged 0 are identified as potential cluster members. Column 6 and 7 show the *Gaia* cross-matched ID and G magnitude. Columns 8 and 9 show $T_{\rm eff}^{p}$ and K_S^{p} data (which includes estimated values for some targets) used to determine $\log L$ and mass. The final column show the probability that the target is a member of its given cluster. Targets with a membership probability of −1 could not be fitted as cluster members. A sample of the table is shown here. The full table is available as supplementary material.

Target cname	cluster DB name	RA (deg)	Dec (deg)	Flag	*Gaia* ID	G (mag)	$T_{\rm eff}^{p}$ (K)	K_S^{p} (mag)	$\log L$	Membership $P_{\rm 3D}$
18331347-1023200	NGC6649	278.30613	−10.38889	0	ID4155024758859315456	16.07	8825	12.53	1.73	0.9199
18331394-1029175	NGC6649	278.30808	−10.48819	0	ID4155014176059792384	16.42	9139	13.07	1.56	0.9917
18331844-1024428	NGC6649	278.32683	−10.41189	0	ID4155017848247221888	15.96	10051	12.60	1.88	0.5234
18331952-1026068	NGC6649	278.33133	−10.43522	0	ID4155017749472616704	16.23	8192	12.59	1.61	0.0000
18332318-1023026	NGC6649	278.34658	−10.38406	0	ID4155024071664517632	16.20	9506	12.85	1.70	0.9898

APPENDIX B: MEASURED DATA AND MODEL FITS

Plots showing histograms of target velocities and the results of the maximum-likelihood analysis for each of the 70 clusters in age order are shown in Appendix B which is available as supplementary material to this paper. A representative set of the four plots is shown for typical cluster in Fig. 6.

APPENDIX C: CLUSTER VELOCITY AND DISPERSION

Plots showing the variation in log likelihood of cluster properties as a function of velocity are shown for each of the 70 clusters in age order are shown in Appendix C which is available as supplementary material to this paper. A representative set of the six plots for a typical cluster is shown in Fig. 7.

APPENDIX D: PLOTS OF CLUSTER MEMBERS

Plots showing properties of potential and likely cluster members for each of the 70 clusters in age order are shown in Appendix D which is available as supplementary material to this paper. A set of the four plots is shown for a typical cluster in Fig. 8.

This paper has been typeset from a TEX/LATEX file prepared by the author.